

Review

Advancements and Challenges in Perovskite-Based Photo-Induced Rechargeable Batteries and Supercapacitors: A Comparative Review

Anil Kumar M. R.¹ , Atiyeh Nekahi¹, Mohamed Djihad Bouguern¹, Dongling Ma²  and Karim Zaghib^{1,*} 

¹ Department of Chemical and Materials Engineering, Concordia University, 1455 De Maisonneuve Blvd. West, Montreal, QC H3G 1M8, Canada; anil.mr@concordia.ca (A.K.M.R.); atiyeh.nekahi@concordia.ca (A.N.); mohameddjihad.bouguern@mail.concordia.ca (M.D.B.)

² Energy Materials and Telecommunications, National Institute of Scientific Research (INRS), 1650 Bd Lionel-Boulet, Varennes, QC J3X 1P7, Canada; dongling.ma@inrs.ca

* Correspondence: karim.zaghib@concordia.ca

Abstract: Perovskite-based photo-batteries (PBs) have been developed as a promising combination of photovoltaic and electrochemical technology due to their cost-effective design and significant increase in solar-to-electric power conversion efficiency. The use of complex metal oxides of the perovskite-type in batteries and photovoltaic cells has attracted considerable attention. Because of its variable bandgap, non-rigid structure, high light absorption capacity, long charge carrier diffusion length, and high charge mobility, this material has shown promise in energy storage devices, especially Li-ion batteries (LIBs) and PBs. This review paper focuses on recent progress and comparative analysis of PBs using perovskite-based materials. The practical application of these batteries as dependable power sources faces significant technical and financial challenges because solar radiation is alternating. In order to address this, research is being performed on PBs with the integration of perovskite solar cells (PSCs) as a way to balance energy availability and demand, cut down on energy waste, and stabilize power output for wearable and portable electronics as well as energy storage applications.



Citation: M. R., A.K.; Nekahi, A.; Bouguern, M.D.; Ma, D.; Zaghib, K. Advancements and Challenges in Perovskite-Based Photo-Induced Rechargeable Batteries and Supercapacitors: A Comparative Review. *Batteries* **2024**, *10*, 284. <https://doi.org/10.3390/batteries10080284>

Academic Editor: Douglas Ivey

Received: 17 June 2024

Revised: 31 July 2024

Accepted: 6 August 2024

Published: 8 August 2024



Copyright: © 2024 by the authors. Licensee MDPI, Basel, Switzerland. This article is an open access article distributed under the terms and conditions of the Creative Commons Attribution (CC BY) license (<https://creativecommons.org/licenses/by/4.0/>).

1. Introduction

The use of energy-based devices by humans is growing, and the diminishing fossil fuel reserves and escalating environmental worries emphasize the need for new energy conversion and storage systems. Global energy consumption by automobiles and the resulting greenhouse gas emissions have been rising rapidly due to economic growth and population expansion [1]. There is a growing need for renewable energy sources due to the ongoing energy crisis and the increasing pollution caused by fossil fuels. The most prevalent clean energy sources are wind and solar power. Energy harvesting technologies like solar cells and wind turbines will become critical to energy production in the future. Battery and capacitor systems, for example, are necessary energy storage devices to utilize the generated electricity [2]. Therefore, the scientific community's top goal is to discover energy storage materials that are reliable, affordable, and efficient. There is a need to better grasp these materials' characteristics, difficulties, and potential future directions to support this endeavor.

Unremitting remote power sources are required for Internet of Things (IoT) devices, smart cities, and other connected devices to enable sensing, data processing, and communication [3–8]. Solar cells and RBs are often used to meet these power needs. Nevertheless, using two different devices leads to redundant parts and more packaging needs, which raises the device's complexity, weight, and expense [9]. This issue is particularly significant as it leads to suboptimal outcomes, primarily due to ohmic transport losses, given

that most of the solar cells exhibit open circuit voltages ranging from 0.6 to 1.0 V, which needs to be improved to effectively charge commercial LIBs. This means that additional stacked cells or DC-to-DC converters are required [1]. Research is still being performed to increase packaging efficiency, such as combining solar cells and batteries into one housing or creating designs that share electrodes between the two [10–13]. Recent advancements in device integration contribute to enhancing gravimetric energy density (GED) and decreasing ohmic transport losses. However, the manufacturing and scientific approach to co-assembling devices still needs improvement. A recent development involves the introduction of photoelectrodes that integrate materials for both Li-ion storage and solar energy harvesting, representing a step towards addressing these challenges [14,15].

To address these issues, a novel material system is required. This is due to the fact that physically combining storage and photovoltaic materials for the implementation of compact devices results in additional fundamental drawbacks. These include reduced charge transport as a result of insufficient material interfaces, energy level discrepancies between the light-absorbing and storage materials, light blockage by the storage medium impeding light absorption, and manufacturing complications like phase segregation [16]. Compact device implementation is a complex task, and its role in addressing these challenges is crucial. Physically combining photovoltaic and storage materials is one approach, but it also has fundamental drawbacks [17–19]. Several factors hinder efficient charge transfer in current systems. These include mismatches in energy levels between light-absorbing and storage materials, light obstruction by the storage medium, inadequate interfaces between materials reducing charge transport, and manufacturing complexities like phase segregation. To tackle these challenges, a novel material system is required [20–22]. RBs and solar cells are usually integrated by connecting two separate devices externally, such as solar rooftops and solar power stations. This setup necessitates the use of additional circuits and electronic components to overcome mismatches between the energy harvesting unit and the energy storage device. These systems are also costly, bulky, and heavy. Combining solar cells and secondary batteries into a single device is another integration technique that can be accomplished with a two-fold active electrode that functions similarly to a battery in terms of both generating and storing solar energy (three-electrode integration) [23].

A three-electrode combination may resolve some of the problems with the four-electrode system. The structure of three-electrode integration is complicated, as is the relationship between the energy-storing and light-absorbing characteristics. Two-electrode integration may be the most appealing approach compared to four and three-electrode systems because of ease of fabrication, compactness, high quality, flexibility, and potential for commercial production [24]. Hodes et al. first proposed photo-RBs in 1976. The two- or three-electrode systems were built on sulfide or selenide compounds. However, challenges such as equipment complexity, low conversion efficiency, and compatibility issues between photoactive and energy storage materials have reduced the progress of rechargeable solar batteries. There is increasing interest in solar rechargeable batteries (RBs) due to the possibility of integrating photo-electrodes into Li-ion, Li-O₂, and Zn-air batteries [25–30].

This perspective will explore the essential characteristics of metal perovskites and incentivize curiosity about the future of energy conversion and storage. We will investigate the interaction between lithium ions (Li-ions) and perovskite crystals, as well as the mechanisms and design of lithium ion (Li-ion) storage in batteries, solar cells, and PBs. We will also discuss the various perovskite materials that are used in batteries, solar cells, and PBs, as well as the developments in contemporary PBs that exhibit dual-functional properties comparable to those of solar cells and batteries. This article will provide an insightful look at the current status of the field and the promising outlook for future advancements.

1.1. Background

As crucial components of contemporary energy systems, solar cells, batteries, and PBs are pivotal in the development of renewable energy technologies, the electrification of transportation, and the widespread use of portable electronics. The achievement of societal

sustainability is contingent on their ongoing and immediate development and integration into a variety of applications.

Perovskite Materials

Perovskite oxide families exhibit a range of simple perovskite oxide forms, with their structural configurations varying based on atomic arrangement within the crystal lattice. These distinctive structural attributes render them captivating, mainly due to their significant utility in storage devices and energy conversion [31].

The perovskite oxide (ABO_3) has a cubic structure, as shown in Figure 1a, consisting of A-cations and B-cations. A-cations are larger and located at the corner sites, with 12-fold cub-octahedral coordination and an atomic position of $(\frac{1}{2}, \frac{1}{2}, 0)$. They typically consist of rare earth metals or group IA or IIA metals. B-cations are smaller and centrally located with six-fold coordination at an atomic position of $(\frac{1}{2}, \frac{1}{2}, \frac{1}{2})$ and can be 3d, 4d, or 5d transition metals.

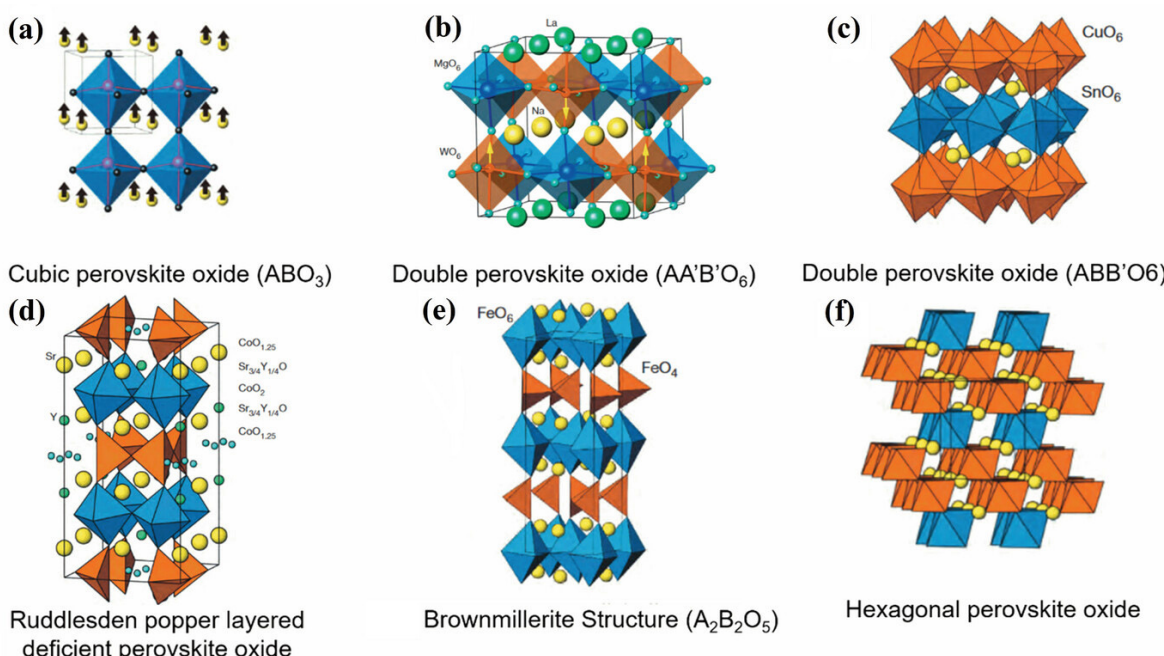


Figure 1. Molecular structures of various perovskite oxides. Reproduced with permission [31]. (a) Cubic (ABO_3), (b) double ($\text{AA}'\text{B}'\text{O}_6$), (c) double ($\text{ABB}'\text{O}_6$), (d) Ruddlesden popper layered deficient, (e) Brownmillerite structure ($\text{A}_2\text{B}_2\text{O}_5$), and (f) hexagonal perovskite oxide.

This adaptability allows the perovskite framework to incorporate more than 90% of the elements, producing various perovskite oxides. Oxygen atoms occupy the face-centered positions. The difference between B and O is $a/2$, and that between A and O is $\sqrt{2}a/2$, where a is the cubic cell parameter. Simple perovskite oxides, including CaMnO_3 , SrMnO_3 , and BaMnO_3 , were investigated by Zhao et al. [32]. Various configurations of octahedron stacking result from variations in the A site, influencing the adsorption characteristics in reactants containing oxygen. Research has demonstrated SrMnO_3 as the most active catalyst in energy-related reactions, indicating the potential of perovskite systems to support adsorption characteristics [33].

Perovskite oxides (ABO_3) can lead to the creation of double perovskite oxides when one cation replaces half of the B site cation. This results in a structure where two different types of cations can occupy the A or B site. The resulting structures can be shown as $\text{A}'\text{A}''\text{BO}_6$ (double A site) and $\text{AB}'\text{B}''\text{O}_6$ (double B site), as shown in Figure 1b,c. Double perovskite oxides are created by expanding the unit of a simple perovskite oxide. In the double perovskite oxide structure, the A and A' cations are located within cub-octahedrons, while the B and B' cations are positioned at the center of an octahedron [34].

The B' and B'' cations play a crucial role in the arrangement of the double perovskite $A_2B'B''O_6$ crystal structure. The three main types are columns, rock salt, and layered B-cation sublattice structures. The specific arrangement is frequently associated with the charge differential (ΔQ) between B' and B'' . A variation of perovskite oxides known as quadruple perovskite oxides is denoted by the symbol $AA'_3B_4O_{12}$. Bochu et al. [35] made the initial identification of these materials. There are two possible structures that can form when another transition metal (called the A' site) fills up 75% of the A site: an A site-ordered quadruple perovskite ($AA'_3B_4O_{12}$) or a 1:3-type A site cation ordering ($AA'_3B_2B'_{16}O_{12}$).

Transition metal ions are arranged in a pseudo-square planar arrangement in the remaining three-quarters of the A site of the $AA'_3B_4O_{12}$ quadruple perovskite oxide structure. In contrast, typical A site ions occupy the remaining quarter of the A site in icosahedral coordination [36]. High-pressure methods are frequently required to synthesize these quadruple perovskites to guarantee that the cation is positioned correctly in the A' site under square planar circumstances. Instead, the B site is adaptable and can hold variability in the cations. A' - B intersite charge transfer is one of the distinctive structural and electronic properties of these structured quadruple perovskites. Ferroelectricity is facilitated by both A and B sites, and the A' - B - B' spin interactions are enhanced, resulting in noticeably high spin ordering temperatures [37–40].

Figure 1d reveals that the layered perovskite oxides of the Ruddlesden–Popper type (RP-type) are a type of perovskite derivative compound. The general formula for these compounds is $A_{n+1}B_nO_{3n+1}$, where $n = 1, 2, \infty$. A periodic sequence of standard ABO_3 perovskite layers interspersed with AO rock-salt layers defines their structural framework. RP-type perovskite oxides have special properties connected to electron and ion transport because of their layered structure. Applications such as solid-oxide fuel cells and metal-air batteries have used their potential. Their broad elemental compatibility, dynamic lattice oxygen, stratified design, and chemical adaptability are the reasons for their versatility [41].

Brown millerite, represented by the formula $AnMnO_{3n-1}$ (which varies from 2 to ∞), is a unique class of perovskite oxides distinguished by their oxygen-deficient nature. As shown in Figure 1e, the architectural design of these structures consists of $(n - 1)$ layers of MO_6 octahedra of the perovskite type interspersed with a single layer of MO_4 tetrahedra rows. This arrangement can also be understood as a perovskite structure with alternating layers of systematically arranged oxygen vacancies [33].

The orthorhombic unit cell of brown millerite can be derived from the base cubic perovskite cell by the following relationships: $a \approx 2\sqrt{ac}$, $b \approx 4a$, and $c \approx 2 - ac$. Because of their unique structural characteristics, brownmillerite oxides have garnered a lot of interest. These include the transition metal's redox activity at the B site and the lattice's flexibility in accommodating additional oxygen atoms. These compounds demonstrate encouraging oxygen permeation, noteworthy ionic–electronic mixed conductivity, and thermal expansion coefficients (TECs) that align with those of traditional solid electrolytes. These characteristics guarantee their strong stability even under harsh oxidative circumstances. These oxides' natural oxygen vacancies intensify catalytic evolution activities [42]. In brownmillerite-type oxides, strong oxide ion conductivity is thus anticipated.

An arrangement of corner-sharing octahedral units characterizes the perovskite structure. Hexagonal perovskites are created when these units share a face. Different hexagonal perovskite derivatives can be produced by combining these octahedral units' corner-sharing and face-sharing configurations, as shown in Figure 1f [43]. The first hexagonal perovskite to be produced that could match other superior solid electrolyte materials in terms of bulk oxide ion conductivity (2.2103 Scm^{-1} at 600°C) was $\text{Ba}_3\text{MoNbO}_{8.5}$. On the other hand, there is still little research on bifunctional oxygen electrocatalysis in hexagonal systems. BaTiO_3 was created by Chen et al. [44] utilizing the Sol–Gel method. Under ideal circumstances, BaTiO_3 showed a tetragonal form, but it lacked electrochemical activity in a vacuum at high temperature (1300°C).

This section focuses on the metal oxides phase, as shown in Figure 2, particularly perovskite crystals crucial to the current research. It includes perovskite materials, ternary

ABO_3 types, solid solutions, and complex compounds. Perovskites with an ABO_3 structure are the most abundant. Their diversity and physical properties accommodate various cations and anion vacancies [45].

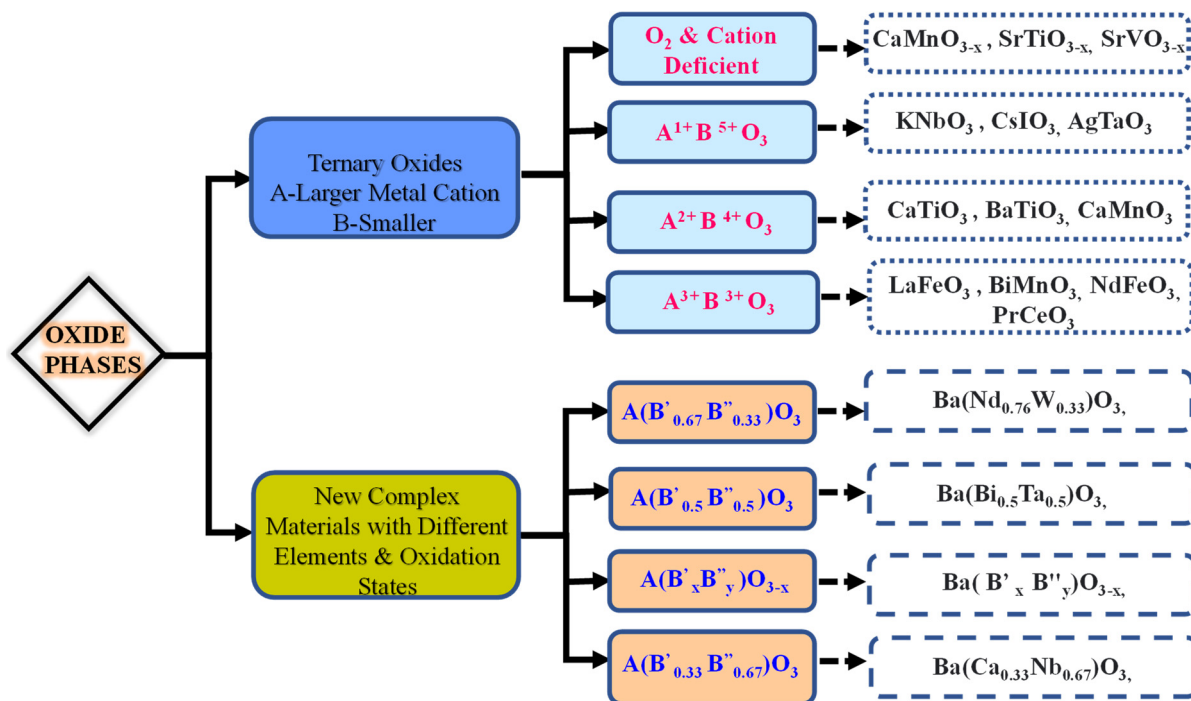


Figure 2. Classifications of oxide perovskite materials.

1.2. Energy Storage Systems

1.2.1. LIBs

Electric energy is frequently stored in batteries for use in electric cars and portable electronics. Electrochemical storage is a promising energy storage technology that offers a lot of potential for creating hybrid energy conversion storage concepts like photo-chargeable batteries [46]. Using extremely pure lithium–metal foil as the anode element and lithium salt in a nonaqueous solution as the electrolyte, a new generation of electrochemical generators was developed in the 1960s. This reaction generates Li^+ ions for charge transport, in contrast to other batteries.



Li metal is lighter, with a molar weight of 6.941 gmol^{-1} and a density of 0.51 gcm^{-3} , showing promise in technology due to its $(\text{He})2s1$ electronic configuration. It has a redox potential of -3.04 V against H_2/H^+ and a specific capacity of 3860 mAhg^{-1} . High electropositivity results in higher voltage compared to other batteries like Ni-metal and lead acid [47]. The development of a passivation layer, which allows ionic transport while hindering direct chemical reactions, has been a significant advancement. Research on lithium batteries began in 1912 under G.N. Lewis through the development of a passivation layer, which permits ionic transport and is thought to be responsible for the stability of lithium batteries [48]. In this field, research has led to the commercialization of various primary lithium batteries. Notable developments include nonaqueous lithium cells, such as the 3-V primary systems, which have been in development since the late 1960s. Examples of these systems are lithium–sulfur dioxide cells, lithium–poly carbon monofluoride cells, and lithium–manganese oxide cells.

Li-Al alloy anode and FeS cathode molten salt systems (LiCl-KCl eutecticum) were introduced a number of years ago [47]. Since their introduction in 1972, lithium–iodine batteries have powered over 4 million cardiac pacemakers and have not been surpassed by

any other electrochemical power source in terms of reliability and performance [49]. An essential factor influencing the properties and operation of LIBs is their cathode materials. In general, they fall into one of three structures, spinel-type (LiM_2O_4), layered ($\text{Li}(\text{M})\text{O}_2$), or olivine-type ($\text{Li}(\text{M})\text{PO}_4$), where M denotes one or more transition metals. The cathode-active materials LFP, LCO, NMC, NCA, LMO, and LNMO are most frequently found in LIBs. Graphite, which comprises approximately 92 weight percent of LIBs (LIBs), is the most widely used anode material due to its strong cycling stability, low cost, natural abundance, high electrical conductivity, and specific capacity of 372 mAh/g. Additionally, silicon oxide (SiO_x), which has a conductivity of about 6.7×10^{-4} S/cm and is inexpensive, environmentally friendly, and naturally occurring, is used by many battery manufacturers. SiO_x is a silicon and carbon blend. When combined with conductive materials, silicon-based materials are frequently used as an extra-active material in LIBs (LIBs) to boost the anode's specific capacity to 3597 mAh/g, which is substantially higher than graphite's capacity of 372 mAh/g [50].

The negative electrode, whether Li metal (a) or a Li insertion compound (b), dictates the operational characteristics of the system. In both scenarios illustrated in Figure 3, the positive electrode consists of an insertion compound where the redox reaction occurs at a high potential versus Li^0/Li^+ . Rechargeable lithium batteries (RLBs) rely on materials that undergo insertion reactions as the electrochemically active component at the positive electrode, marking a critical advancement in battery technology, which started in the 1970s. Two distinct methodologies are employed in RLB design, as illustrated in Figure 3. In the first system, the positive material is an insertion compound, and the negative electrodes are metal foil and lithium (Figure 3a). Li-ions are moved from one intercalation compound that supplies Li-ions to another that receives them during the discharge process and vice versa in the second system, which uses two open-structured materials as electrodes. This is the Li-ion battery type that is frequently used, as seen in Figure 3b [51].

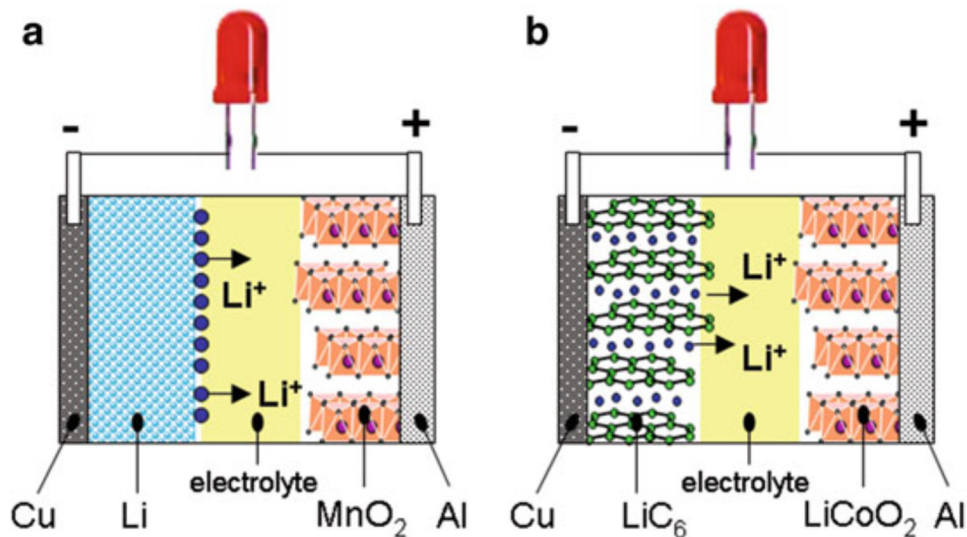


Figure 3. Schematic representation of LIBs. Reproduced with permission from reference [52].

1.2.2. SCs

SCs are electrochemical energy-storage devices with high power rates means and can store and release energy quickly. SCs are formed by two electrodes connected by an electrolyte and separated by an ion-permeable membrane acting as a separator. Because of their easy-to-charge separation energy storage mechanism, they are also referred to as power capacitors, ultracapacitors, or electrochemical capacitors [53,54].

Batteries have an energy storage capacity three to thirty times greater than that of SCs [55]. Rather than being used for long-term energy storage, are used when rapid cycles of charging and discharging are required. Consequently, SCs find application in

regenerative braking, burst-mode power delivery, cars, trains, cranes, and lift systems and are also used in emergency doors on the Airbus A380 [56–58].

SCs have a lower power output (approximately 10,000 W/kg) than conventional capacitors (electrolytic or electrostatic capacitors). Because of the minimum distance in the EDLC between opposite charges and the highly porous electrodes that are usually used, SCs have a significantly higher capacitance than conventional capacitors. Therefore, the properties of the porous carbon electrodes have a direct bearing on their power and energy-storage capacities [59–61]. SCs have an energy density higher than capacitors but lower than batteries, placing them in the middle of the two types of capacitors, and they have a higher power density than batteries but lower than conventional capacitors. The power densities of conventional capacitors are comparatively higher. They do not, however, have as high an energy density as batteries or electrochemical capacitors. Hence, batteries have a greater energy storage capacity than capacitors but a slower rate of electrical energy delivery. This suggests that a battery has a low power density. On the other hand, compared to batteries, capacitors typically store less energy per unit volume or mass; however, this energy can be rapidly released, yielding a significant amount of power. As a result, a capacitor's power density is typically very high. The Ragone plot in Figure 4 is a key tool in understanding the power/energy relationships between lithium-ion batteries, SCs, and conventional capacitors. While it provides a comprehensive view, it is important to note that it does not encompass all aspects of performance.

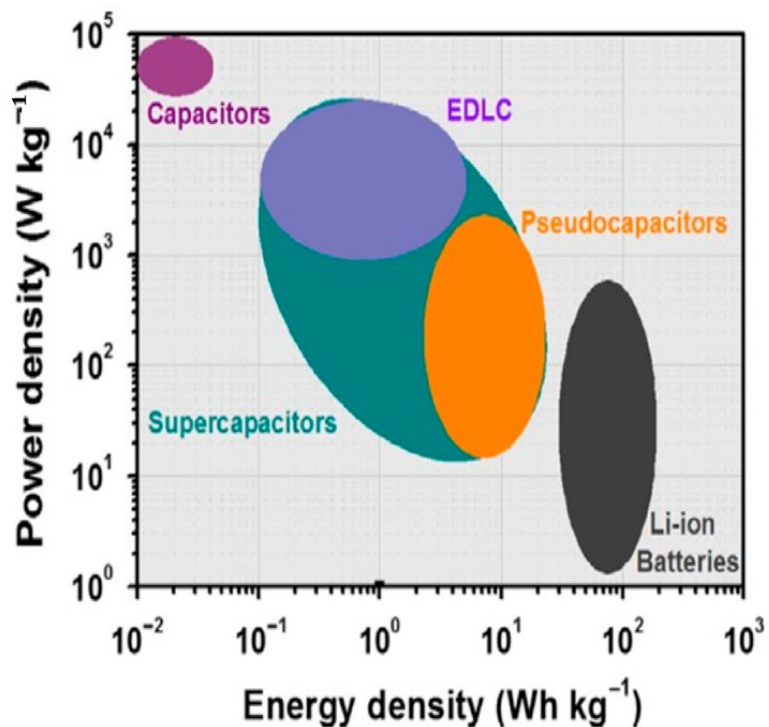


Figure 4. A Ragone plot demonstrating the power density against the energy density of energy storage devices. Reproduced with permission from reference [62].

SCs are categorized based on the energy storage pathway into electrical double-layer capacitors (EDLCs), hybrid capacitors, and pseudocapacitors, as shown in Figure 5. Pseudocapacitors store energy through fast faradaic redox reactions, resulting in higher specific capacitance and energy densities compared to EDLCs. They utilize conducting polymers and metal oxides like transition metal oxides, sulphides, selenides, and nitrides. On the other hand, EDLCs excel in power and cyclic stability. Hybrid capacitors are a special type formed by combining non-faradaic EDLCs and faradaic pseudocapacitors. The power and cyclic stability of EDLCs are good, but the specific capacitance value of

pseudocapacitors is high. When non-faradaic EDLCs and faradaic pseudocapacitors are combined, a unique type of supercapacitor known as a hybrid capacitor is produced [63,64].

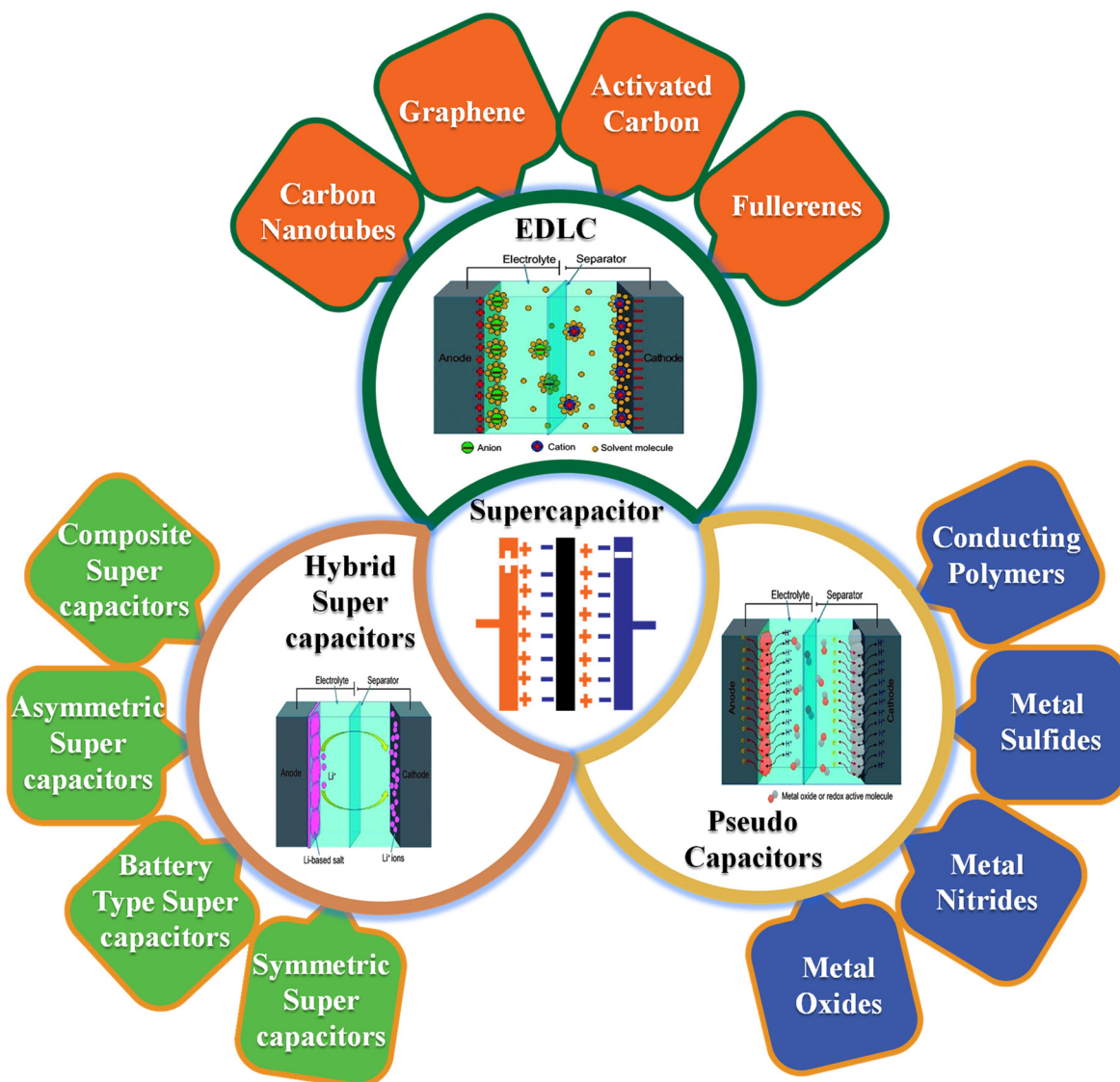


Figure 5. The classification of SCs based on active materials [63,64].

EDLCs are made possible by both electrostatic and non-faradaic processes, resulting from charge accumulation at the electrode–electrolyte interface. Carbon-based materials like carbon nanotubes, graphene, and activated carbon are commonly used as electrodes in EDLCs due to their large surface area, high conductivity, and stability at high temperatures. While EDLCs have high power density and excellent charge–discharge cycling stability, they suffer from low energy density and small specific capacitance. Strategies such as increasing conductivity and controlling surface area and pore size are crucial for achieving high capacitance in EDLCs [53,65]. To achieve our goal, there is a need to review battery and solar cell technologies and identify specific components that can be combined into a single device for optimal performance. This will increase complexity, but by defining our research boundaries and leveraging advancements in these industries, we can develop groundbreaking technologies [66–69].

1.2.3. PBs

Because sunlight is intermittent, solar cells require energy storage devices, like batteries, to store electrical energy and stabilize their power output. Combining energy storage and harvesting into one unit can improve volumetric performance and provide a number of benefits. PBs are the name given to these integrated devices. Hodes et al. [24] first proposed the idea of a combined two- and three-electrode photoelectrochemical cell (PEC) and photoelectrochemical storage cell (PESC) in 1976. In this case, the photoelectrode was made of 2 cm^2 Cd-Se on a conducting base and was heat-treated in an inert atmosphere. Potentials between 450 and 560 mV were measured in 1 AM sunlight using a Cd-Se electrode, with currents between 7 and 10 mAcm^{-2} and open circuits, and the schematic representation of the two- and three-electrode PESCs is shown in Figure 6. In 1981, Hada et al. conducted an investigation on the two-compartment PESC. The study utilized platinum (Pt) as a counter and storage electrode, titanium oxide (TiO_2) as a photoelectrode, and aqueous solutions such as $\text{Ce}(\text{SO}_4)_2/\text{Ce}_2(\text{SO}_4)_3$ with a HNO_3 electrolyte. Additionally, the Pt storage electrode was immersed in aqueous AgNO_3 solution with a KNO_3 electrolyte [70].

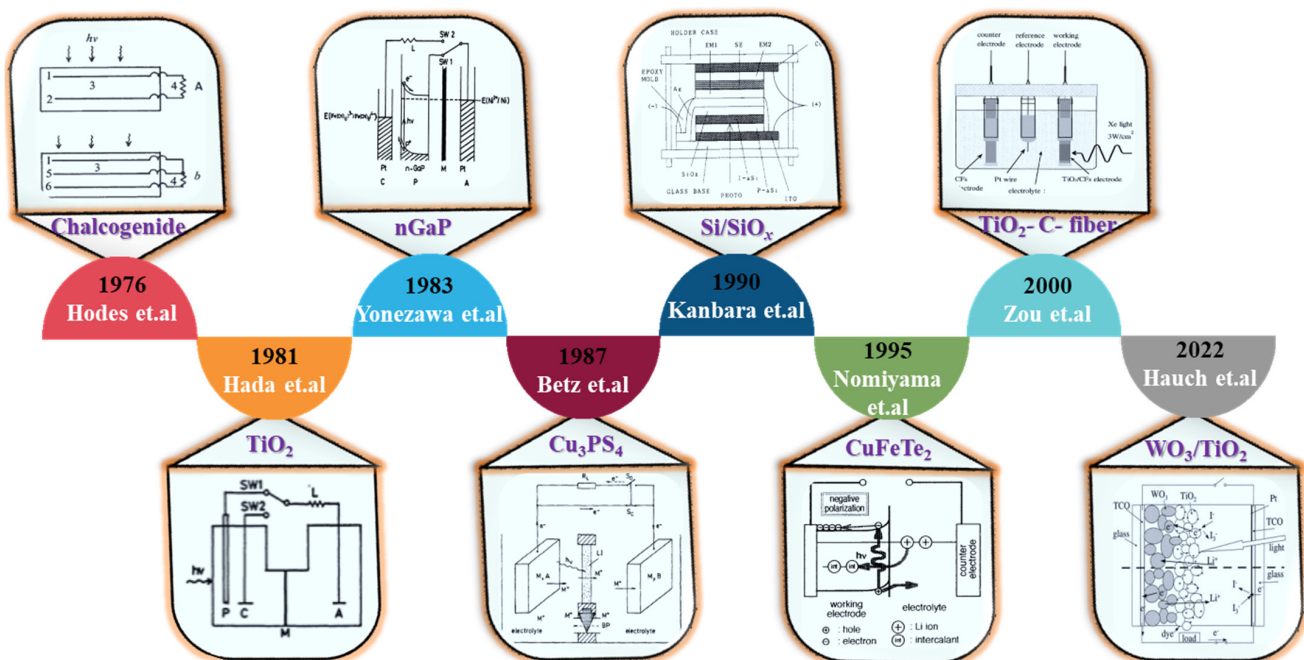


Figure 6. Progress of photo-RBs: history from 1976 to 2022.

The configuration was referred to as a solid-state photogalvanic cell since the two compartments were divided by a membrane that was specific to anions. The cell was charged using ultraviolet light with a wavelength of 300–400 nm directed at the photoelectrode. A similar method was employed [71] in 1983 but involved the use of a different photoelectrode (n-GaP) and aqueous electrolytes like $\text{K}_3[\text{Fe}-(\text{CN})_6]/\text{H}_4[\text{Fe}(\text{CN})_6]$ with NiSO_4 solution within a pH range of 6.5 to 9.5. In an attempt to increase the power efficiency of the photo-battery by using a n-GaP photoanode, 2% storage efficiency was attained with a potential of -1.0 V for the n-GaP electrode at the pH of 1 and a standard potential of 0.36 V against the normal hydrogen electrode. Additionally, the Ni^{2+}/Ni electrode (-0.25 V) was selected against the normal hydrogen electrode.

A study on charge storage with the p-type semiconductor photocathode Cu_3PS_4 (2.3 eV energy gap) was carried out in 1987 [72]. The electrolyte in the system was a CuCl solution, the reference electrode was Pt, and the counter electrode was a copper wire. When the photocathode and electrolyte interface were exposed to light, the photogenerated Cu^+ cations underwent a reaction that produced a photo potential. This reaction produced an open circuit voltage (OCV) of 180 mV and a photo potential of 40 mV. Using a blend

of $\text{Ag}_{0.7}\text{V}_2\text{O}_5$ and $\text{Ag}_6\text{I}_6\text{WO}_4$ as the counter electrode and a p-type a-Si/intrinsic a-Si coated with a SiO_x layer as the photoelectrode, Kanbara et al. (1990) prepared a solid-state photoelectrochemical (PEC) system. Even after 900 cycles, this system showed good stability with an OCV of 0.3 V [73].

There are two components to the cell. The first is an MIS-type photovoltaic component made of ITO/(P-I aSi)/SiO_x/Ag (100 mg of $\text{Ag}_{0.7}\text{V}_2\text{O}_5 + \text{Ag}_{614}\text{WO}_4$ weight ratio of 3:2), and the Ag layer was created in 2000 via vacuum evaporation using 500 mg of $\text{Ag}_{614}\text{WO}_4$ and 300 mg of $\text{Ag}_{0.7}\text{V}_2\text{O}_5 + \text{Ag}_{614}\text{WO}_4$ weight ratio of 3:2. SiO_x thickness and the three-layered EM1 structures. Similarly, Nomiyama et al. [74] studied the CuFeTe₂ layer structure of the photo-charging effect in 1995. All measurements were made using a CuFeTe₂/LiClO₄/Pt system under Xe lamp (500W) irradiation, utilizing a three-electrode method. The cell consists of two separate compartments connected by a salt bridge. One compartment contains nonaqueous solution and the other contains a working electrode, a counter electrode (a platinum plate), and an electrolyte (0.5 M acetonitrile). The other compartment contains the reference electrode (Ag:AgCl) and an electrolyte (saturated KCl solution).

In 2000, researchers developed TiO₂ and a bundle of carbon fibers (CFs) and utilized them as a layered material and photocatalyst, respectively, resulting in an energy density of 0562 Wh/kg from photocharging. Subsequently, TiO₂/CF composite electrodes have been manufactured using the sintering technique [75], which involves applying a diluted TiCl₄ acetonitrile to CFs and then sintering the CFs in air to create TiO₂ particles on their surface. For practical use, their photo-charged quantity was, however, relatively small. This can be explained by the large size (one-liter diameter) and low density of the TiO₂ particles. To achieve high opto-electric conversion efficiency, TiO₂ particle density and specific surface area on CFs must be increased in order to increase light absorption and enlarge the interface.

Finally, researchers built 5 μm thick TiO₂ and 25 μm thick WO₃ layers and applied them to the substrate in 2002 [76] through the Sol-Gel method using doctor-blading. The idea is to incorporate an additional layer (WO₃) that can capture the energy generated by the solar cell as a secondary redox pair. As the reduction potential for Li⁺ intercalation of WO₃ is close to 0 V versus a standard hydrogen electrode, it is appropriate for a dye-sensitized solar cell's potential. The redox potential of the I⁻/I₃ couple in this type of cell is approximately 0.53 V versus hydrogen, and the open-circuit potential of the dye-sensitized TiO₂ layer versus the I⁻/I₃ couple on the Pt electrode is about 0.7 V. In an hour, this system could store 1.8 C/cm² of charge under 1000 Wcm⁻² of illumination. Figure 6 presents the evolution and development of all photo-RBs from 1976 to 2022.

2. Working Mechanism

2.1. Mechanism of Solar Cells

The semiconductors utilized in the construction of a solar cell consist of p-type and n-type layers. In most commercial solar cells, a hole, which is an electron vacancy, is formed in the p-type layer.

To create n-type silicon, atoms like phosphorus, with an extra electron in their outer level, are used. Phosphorus forms a bond with silicon, allowing the extra electron to move freely. In a p-n junction, the p-type layer has positively charged holes while the n-type layer has excess electrons. When they come into contact, electrons from the n-type layer move to the p-type layer, forming a depletion zone with charged ions. This zone creates an internal electric field that prevents further electron movement between the layers as shown in Figure 7.

A p-N junction semiconductor produces electron-hole pairs, which are charge carriers, when sunlight strikes it. An electron travels from the valence band (E_v) to the conduction band (E_c) upon absorption of a photon with energy greater than the material energy gap, leaving a hole in the valence band in its wake. Any extra energy from the photon that is absorbed gives the electron or hole more kinetic energy. The symbol “hv₀” stands for the

minimum energy needed to form an electron-hole pair in a semiconductor. The surplus energy in the semiconductor is released as heat.

In practical applications, multiple solar cells are connected in parallel and series to create solar panels. A single PV cell typically generates around 0.5 V, so connecting cells in series, such as six cells, can increase the voltage. Additionally, linking cells in parallel can increase current capacity. For example, connecting 12 cells in a series-parallel configuration should produce 4 A at 3 V, assuming that 6 cells alone would only produce 2 A [77,78].

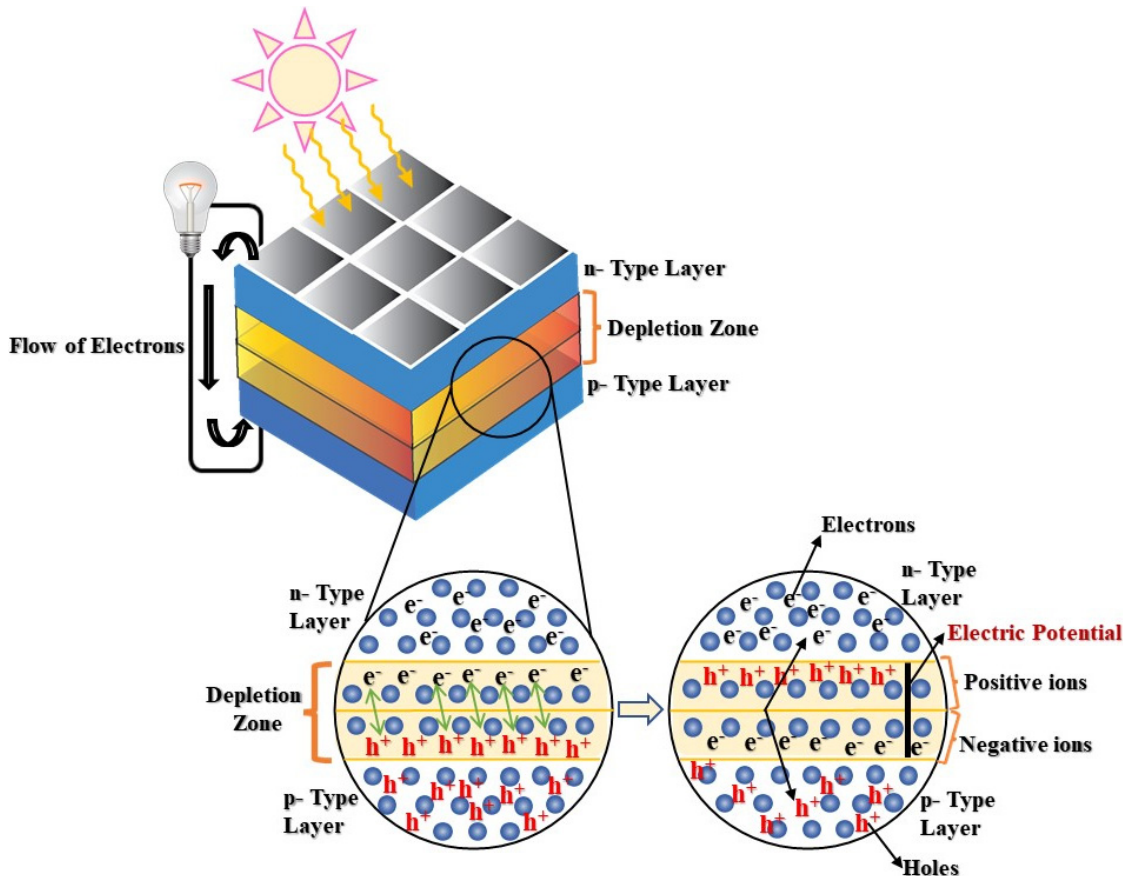


Figure 7. Mechanism of solar cells.

2.2. Mechanism of LIBs during the Charging and Discharging Process

Rechargeable lithium batteries (RLBs) were developed in the 1970s as a result of materials undergoing insertion reactions as the electrochemically active component at the positive electrodes. RLBs employ two different techniques: the first system uses an insertion compound, sometimes referred to as a lithium–metal battery, as the positive material and a lithium–metal foil as the negative electrode. Li-ions can move between the two open-structured materials used as electrodes in the second system as the discharge process progresses. Originally known as a “rocking chair battery”, “swing battery”, or “shuttlecock battery”, this type of battery is now commonly referred to as a Li-ion battery. LiBs can also be referred to as lithium metal-free RBs [51]. LIBs (LiBs) primarily contain charge species Li^+ ions. These ions oscillate between the electrodes in the electrolyte, which functions as an electrical insulator and an excellent ionic conductor. A new cell is at low potential or in the discharge state (Figure 8b). As a result, in the initial state, the anode (carbon) is empty, and the positive electrode (Li_1CoO_2) is packed with Li^+ ions. The movement of ions and electrons is a necessary component of any electrochemical reaction, and this is how the redox process works in a LiB.

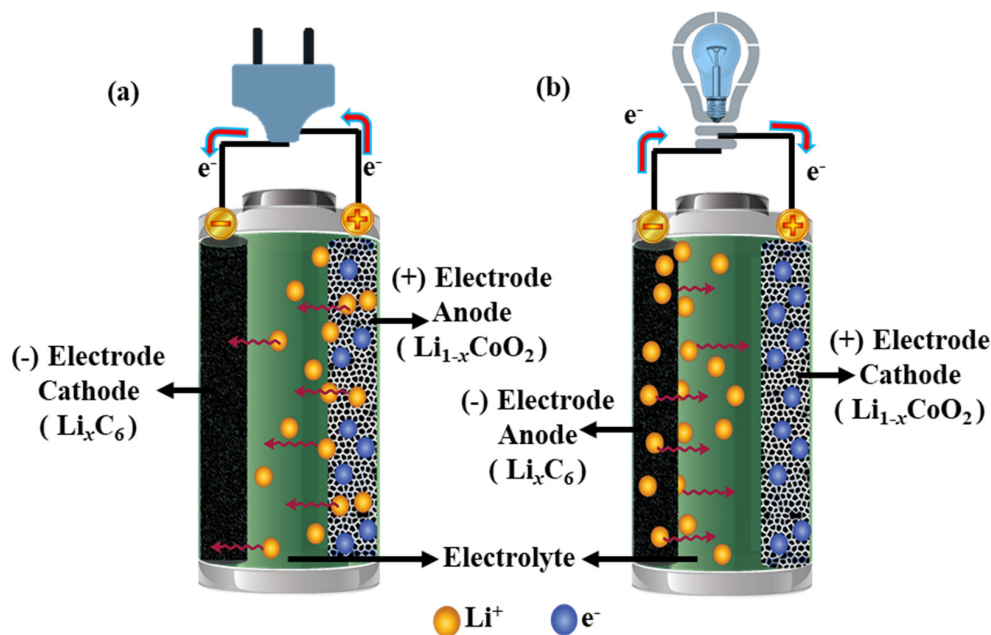
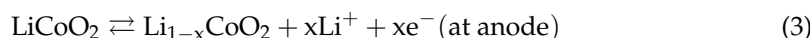
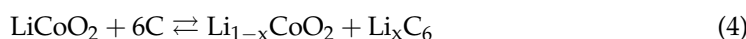


Figure 8. Working principle of a Li-ion battery: (a) charging process and (b) discharging process.

Li-ions are produced at the positive electrode (anode) and travel through the electrolyte to the negative electrode (cathode) during the charging process (see Figure 8a). Electrons move through the external circuit simultaneously. While the negative electrode is oxidised and loses x electrons ($\text{Li}_{1-x}\text{CoO}_2$), the positive electrode is reduced and captures x electrons (Li_xC_6). The following chemical reactions occur during the charge and discharge of a Li-ion battery (LIB) with graphite-like carbon serving as the negative electrode and LiCoO_2 serving as the positive electrode. The operating mechanism of the LIB is also illustrated in Figure 8a,b.



where the charge process is represented by the lower arrow and the discharge process by the upper one. The battery's overall response is stated as follows:



But some amorphous materials can be employed, and more research is being performed in this area, especially with regard to some anode materials [79].

LIBs (LiBs) mainly consist of Li-ions as the charge species. These ions move back and forth between the electrodes in the electrolyte, with lithium hexafluorophosphate (LiPF_6) salt currently being the primary electrolyte used in LIBs. LiPF_6 , one of the salts used in this mixture, has been recommended because of its capacity to improve conductivity and passivate aluminum collectors. LiPF_6 , however, can break down and is thermally unstable, which can have negative consequences. Additionally, it can react to form HF with leftover water. Lithium imide salts, such as LiTFSI , could be used in place of LiPF_6 to solve these problems. Although LiTFSI is thought to be safer and more stable, there are worries that it might cause aluminum collectors to corrode. Numerous investigations have been carried out to understand this phenomenon [51,80].

Nanotechnology reduces the size of active particles in electrode design, which shortens the time a guest species must pass through a solid during discharge–charge cycling [81]. For safe public transit, LiBs with titanate and iron phosphate electrodes pass battery tests. The battery pack's cells are balanced by the BMS (Battery Management System). With a 95% capacity retention at 100% DOD and SOC, the 800 mAh battery can withstand 20,000 cycles.

at a 10C charge rate (6 min) and 5C discharge rate (12 min), as well as 30,000 cycles at a 15C charge rate (4 min) and 5C discharge rate. Commercial batteries have incorporated several novel cell chemistries developed since LiBs with LiCoO_2 as the oxidant electrode were first introduced [82].

2.3. Mechanism of the Photo-Battery

These photoelectrons accumulate on the counter-electrode through the external circuit (Figure 9a, photocharging). Our hypothesis states that Li-ions are repelled out of the perovskite matrix by the photogenerated holes during low discharge, which occurs when the battery is in the intercalation regime. As seen in Figure 9a, this procedure enables the battery to start photocharging. Perovskite and rGO/PCBM work together to form broad conducting pathways that cross grain interfaces and boundaries. But for the majority of them, recombination or trapping occurs due to the short carrier lifetimes (approximately 200 ps) and short diffusion lengths (less than 100 nm) of electrons and holes in perovskites. Some recharging at lower discharges in the conversion region (Figure 9b, photo discharging). This could be explained by residual intercalation effects or by the photogenerated holes reacting with lithium iodide (LiI) to form Li^+ .



As shown in Figure 9, the accumulated photoelectrons ($\text{Li}^+ + e^- \rightarrow \text{Li}$) at the counter electrode further reduce the Li^+ , balancing the total photogenerated carriers and causing photocharging of the battery [83].

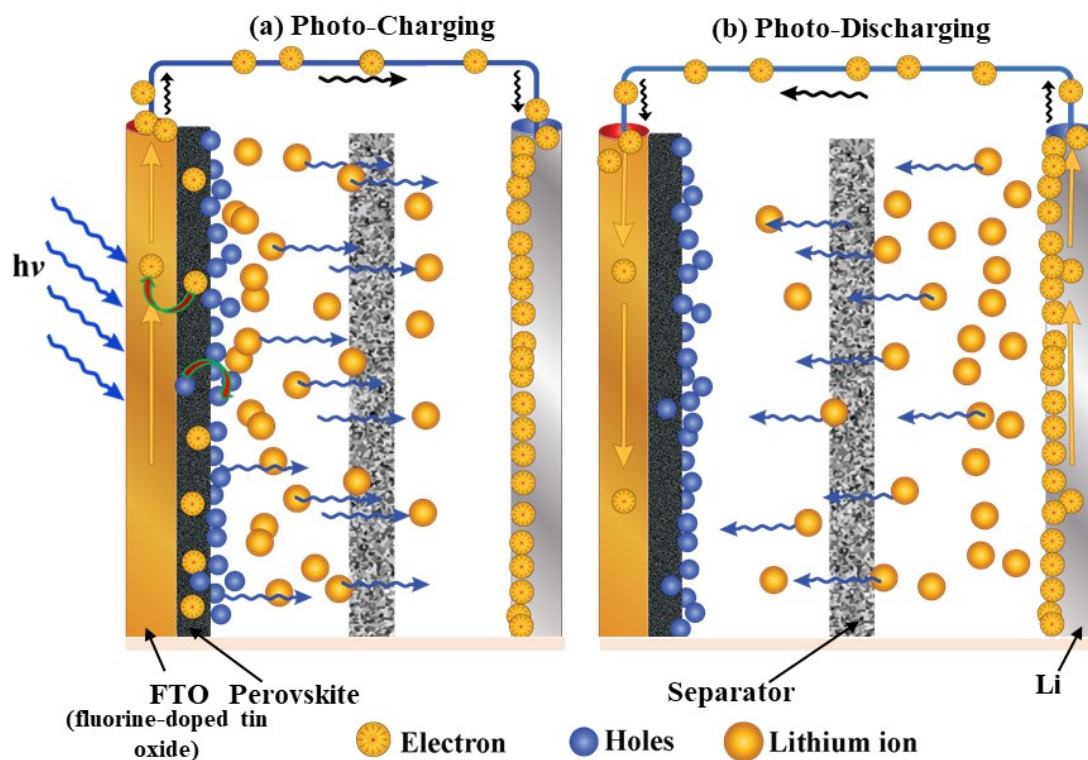


Figure 9. Schematics storage mechanisms of the perovskite photo-batteries: (a) photo charging and (b) photo discharging [84].

A $\text{LiI} // \text{Li}_2\text{WO}_4$ redox flow battery was designed utilizing a LISICON permeable membrane and a $\text{TiO}_2/\text{N}_{719}$ dye photoanode. In the process of photo charge reaction, Li-ions are intercalated in Li_2WO_4 by the injection of photogenerated electrons from N_{719} into the titania band. This reaction causes the oxidation of iodide ions at the photoanode. Under lighting conditions, the battery was able to achieve 0.76 V in just 2 min, indicating the

oxidation of I^- into I^{3-} . Moreover, the battery exhibited high-capacity retention, exceeding 90%. In a similar experimental setup, some researchers introduced a lithium metal anode to enhance the battery's energy density [85,86]. Through the utilization of an N719/TiO₂ couple and iodide as the redox mediator, it was observed that a light source could decrease the charge voltage of a lithium-air battery [28].

Li₂O₂ oxidation potential dropped from 3.4 V to 2.8 V when exposed to light. This setup used the potential difference between the air and lithium metal electrodes to function as a regular lithium–air battery during discharge, so the air electrode and the photoelectrode were kept apart. By establishing a potential between the photo-electrode and the lithium electrode, photo-assisted charging was accomplished. This resulted in the formation of I^{3-} species close to the photo-electrode, which decreased the Li₂O₂ discharge product from the air electrode. Furthermore, by depositing the g-C₃N₄ photocatalyst on the air electrode surface, it was possible to further reduce the Li-air battery's charge potential to 1.9 V while still providing 0.01 mA of charge [87]. This demonstrated the creation of a functional two-electrode photo-assisted lithium-air battery.

Li et al. [87] developed a solid, flexible lithium-air battery that uses photoassistance. This novel battery is composed of a pre-lithiated silicon anode, an electrolyte containing 5% mol LiTFSI in succinonitrile, and an air electrode coated with “ZnS-CNT” that is photosensitized with carbon paper or carbon textile. Despite the unconventional nature of the photo-sensitive “ZnS-CNT” mixture, which consists of ZnS nanoparticles and carbon nanotubes (CNTs) rather than a conventional smooth layer of ZnS deposited on CNTs, this battery demonstrated excellent capacity stability. After at least 50 cycles at 0.026 mA cm⁻², the light-assisted charge potential rose from 2.08 V to 2.2 V. Furthermore, the charging voltage was decreased to roughly 2 V by the photo-sensitive coating.

In their study, Wang et al. [88] utilized WO₃-CdS-TiO₂ as a photoanode, operating at a general voltage of approximately 0.6 V. CdS generated photoelectrons that facilitated the reduction of WO₃ through a TiO₂ connection, while I was oxidized to I^{3-} . However, CdS deterioration occurred due to the formation of SO₄²⁻-based side products and an elemental sulfur intermediate, resulting in the non-reversible cycling of the battery. Doukouzkis et al. [89] used WO₃ and a cobalt species (Co(II)(bpy)₃(PF₆)₂) as the hole acceptor in a lithium intercalation/de-intercalation reaction in a photoelectrochromic cell that was similar to this one. By placing a ZnS interlayer on the working electrode, the authors were able to reduce the Co-redox shuttle's recombination losses in comparison to the typical I^-/I^{3-} .

3. Materials Demand

The widespread adoption of clean energy, including solar PV and batteries, is driving remarkable growth in the critical minerals market. The demand varies based on the resources, their availability as reserves, and their contribution to preventing the dominance of some countries and making a reliable source [90]. These elements are categorized by the used technologies, which are related to this article comprising solar PV (Figure 10a,b), electric vehicles (Figure 10c), and grid battery storage (Figure 10d). Indeed, the same elements will not be used in the photo-batteries as well, but we aim to cover all of the demand in the categories of PSCs, batteries, and combined systems. For such analysis, we utilized IEA's data explorer to gather quantitative data on the demand for critical materials. Demand was represented under various scenarios and varies mainly based on technology evolution trends. Despite this, these numbers and trends will be constantly updated to stay in alignment with the latest projections in the energy domain [91]. In the batteries sector, electric car sales surged by 60% in 2022, exceeding 10 million units, and energy storage systems doubled in capacity. Between 2017 and 2022, the energy sector significantly boosted overall demand, tripling for lithium, rising by 70% for cobalt and 40% for nickel. In 2022, the share of clean energy applications in total demand reached 56% for lithium, 40% for cobalt, and 16% for nickel, compared to 30%, 17%, and 6% in 2017, respectively [92]. EV domain forecasted (Figure 10c) a demand of 349 kt Li, 113 kt Co, and 1497 kt Ni in 2030,

with a striking enhancement toward 907 kt Li, 212 kt Co, and 3040 kt Ni in 2040 and 1039 kt Li, 295 kt Co, and 3272 kt Ni in 2050 (APS).

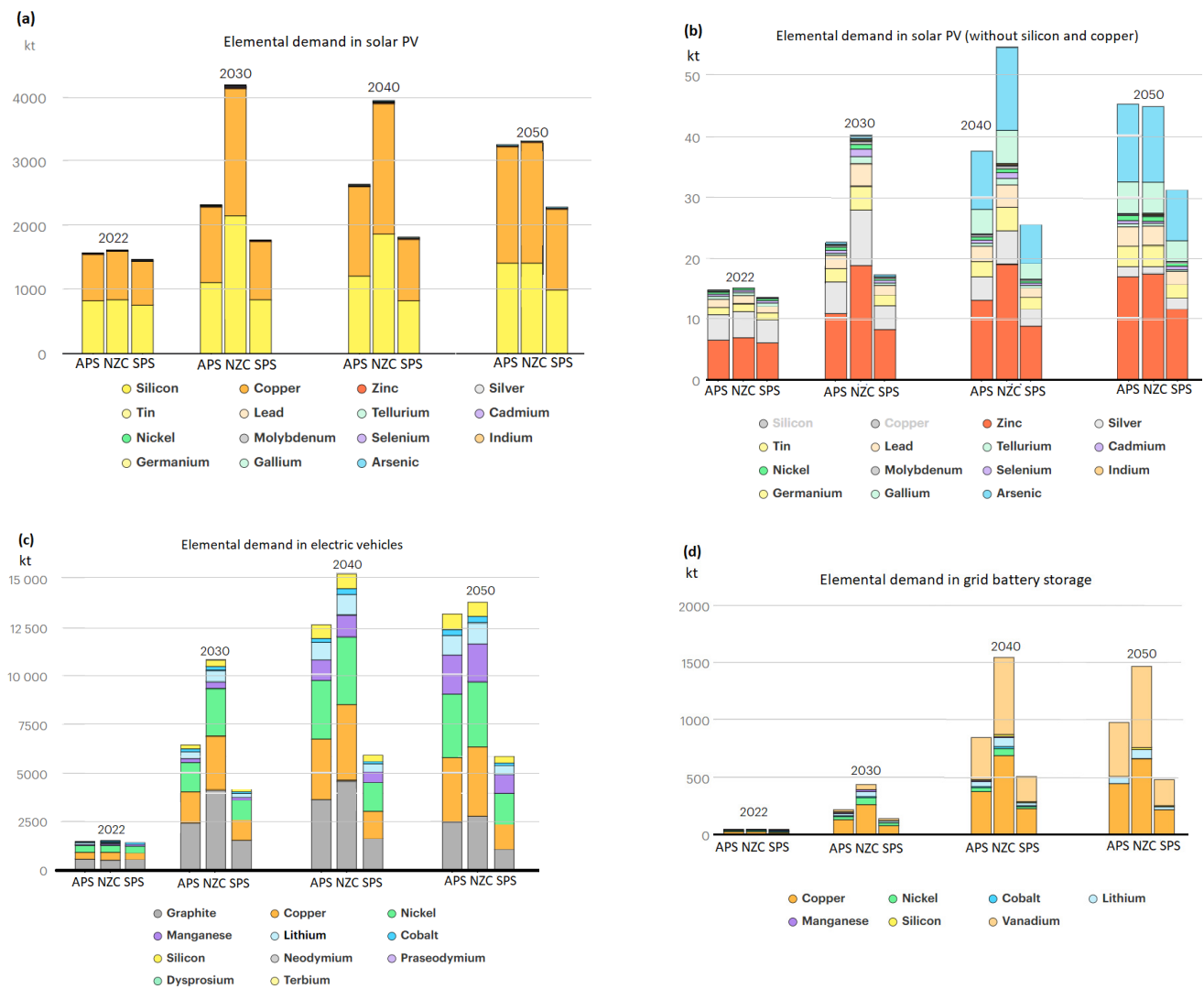


Figure 10. Elemental demand in various technologies: (a) solar PV, (b) solar PV with a better representation of other elements than copper and silicon, (c) electric vehicles, and (d) grid battery storage. The forecast for 2030, 2040, and 2050 is represented based on various scenarios of Announced Pledges Scenario (APS), Net Zero Emissions by 2050 Scenario (NZS), and Stated Policies Scenario (SPS). All data were obtained from IEA and the graphs were produced using IEA's Critical Minerals Data Explorer [90].

In 2022, global renewable energies hit a spending record of USD 600 billion for 340 GW capacity, led by strong growth in solar PV. China contributed nearly 100 GW, a 70% increase from 2021, with plans for another 150 GW in 2023. The EU saw a 50% rise in solar PV additions, driven by increased renewables investment amid cuts in gas deliveries [93]. As is shown in Figure 10a, there was a huge demand for silicon and copper in the realm of solar PV technology in 2022 (816 kt and 731 kt, respectively), surging to 1108 and 1176 kt in 2030 and 1402 and 1811 kt in 2050, respectively (APS). Zinc and silver are placed in the next rank of demand in 2022, with huge growth for arsenic from 2040 (Figure 10b) (APS). Notably, silver has experienced a declining trend in growth, and lead and tin have shown a slight increase despite a striking growth in entire demand up to 2050. Instead, arsenic and gallium are expected to have an upward trend starting from 2035, with 0.68 kt Ga and 1.68 kt As to 5.13 kt Ga and 12.83 kt As in 2050.

4. Technological Challenges and Opportunities

4.1. Design of PSCs

The design of PSCs is similar to that of organic dye-sensitized structures, but the photoactive layer in PSCs sets them apart from the latter. PSCs feature a photoactive layer composed of metal-halide perovskite, similar to the organic semiconductor in organic dye-sensitized structures. As seen in Figure 11, this active layer in PSCs is typically located between an electron transport layer (ETL) and a hole transport layer (HTL). The layered PSC structures can be made of different materials, including liquid electrolyte dye-sensitized, mesoporous structured, planar structured, inverted structured, HTL-free, and ETL-free solar cells [93].

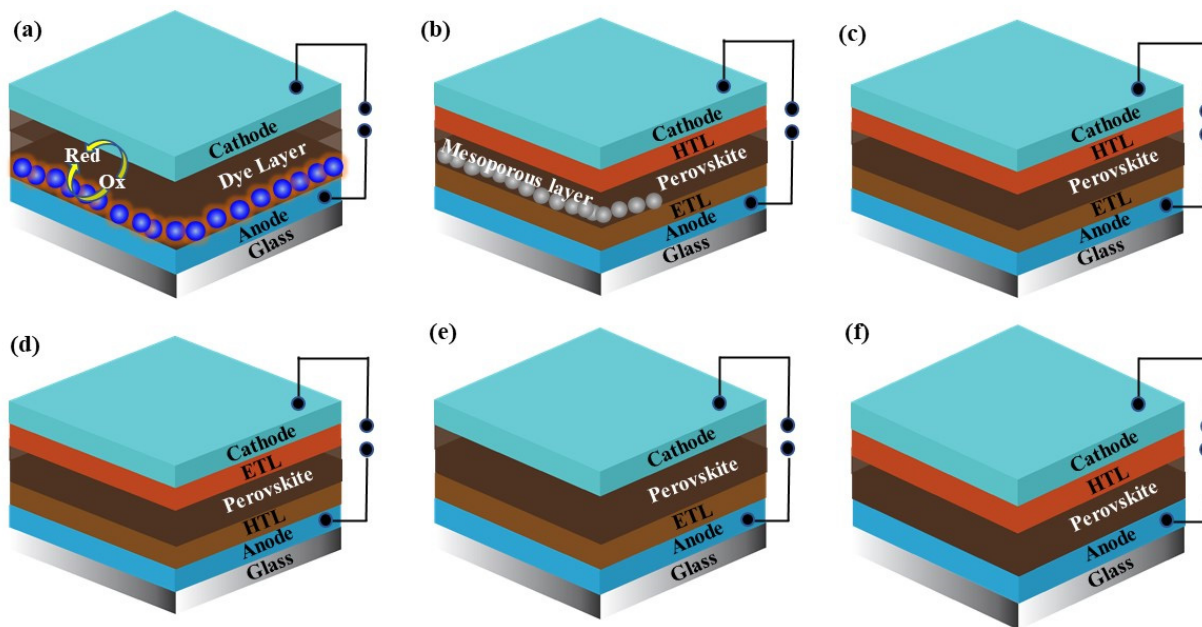


Figure 11. Various designs of PSCs: (a) dye-sensitized solar cell; (b) mesoporous structured solar cell; (c) planar structured solar cell; (d) inverted structured solar cell; (e) HTL-free layered solar cell; (f) ETL-free layered solar cell [93,94].

Interfacial fracture toughness is essential to improving the efficiency and dependability of recently created solar cells. There are several techniques that have been used to quantify interfacial fracture toughness using a single mixed mode, including micro-scratch, peel, and bulge tests. Even though photovoltaic photonic strip circuits (PSCs) are expected to surpass 25% in power conversion efficiency (PCE) by 2020, adhesive and cohesive fracture resistance (G_c) values for solution-processed devices are currently less than 1.5 J/m^2 [93]. Furthermore, different modes can be used to assess interfacial fracture toughness in order to capture significant energy release rates, especially for thin film interfaces. These findings give hope for more advancements and progress in the field of PSCs by pointing to possible future research directions.

A transparent conducting oxide substrate (TCOS), nanoporous TiO_2 , an electrolyte, a perovskite sensitizer (dye layer), and a metal counter electrode are the various parts of dye-sensitized solar cells, as shown in Figure 11a. For instance, $\text{CH}_3\text{NH}_3\text{PbBr}_3$ was used as the sensitizer for TiO_2 in early dye-sensitized solar cells, resulting in a power conversion efficiency (PCE) of 2.2% [95]. Subsequently, using $\text{CH}_3\text{NH}_3\text{PbI}_3$ as the sensitizer resulted in a PCE of 3.8% [96]. The iodide absorber led to a higher short-circuit current density (J_{sc}) due to a broader absorption spectrum and lower bandgap. After optimizing the synthesis of $\text{CH}_3\text{NH}_3\text{PbI}_3$ and TiO_2 nanoparticles, researchers achieved 6.5% power conversion efficiency (PCE) [97]. However, the extreme instability of liquid electrolyte dye-sensitized cells led to an 80% decrease in PCE within 10 min, and the challenge of finding a stable

liquid electrolyte halted further research on these cells. It was noted that the free energy generated from chemical reactions in these cells could potentially lead to a battery-like effect, possibly increasing the output power [94].

Mesoporous cells typically consist of a metal electrode, a TCOS, an HTL, a mesoporous scaffold made of TiO_2 or Al_2O_3 , the perovskite absorber, and the HTL (Figure 11b). The perovskite layer's surface coverage, homogeneity, roughness, and other properties have a significant impact on the device's performance. Using a solid-state hole transport material (HTM) known as 2,2',7,7'-tetrakis (*N,N*-di-*p*-methoxyphenylamine)-9,9'-spirobifluorene (spiro-OMeTAD) [98], Kim et al. were able to successfully fabricate the first solid-state PSCs. Recently outperformed other materials with FAPbI₃ cells prepared via an intramolecular exchange method, achieving a certified higher power conversion efficiency (PCE) of 20.1% [99].

A cell with no mesoporous layer is referred to as having a planar heterojunction structure. An arrangement of functional layers in the device—beginning with the layer that is exposed to light—determines whether a cell structure is classified as n-i-p or p-i-n. The general design of planar n-i-p PSCs is depicted in Figure 11c. PSCs with a planar structure of FTO/compact TiO_2 /perovskite/spiro-OMeTAD/Au were first reported by Ball et al. [100]. Studies have demonstrated that planar heterojunction PSCs outperform PSCs made of other materials, with a power conversion efficiency (PCE) of 19.3% when annealing $\text{CH}_3\text{NH}_3\text{PbI}_3$ films in an environment with $30 \pm 5\%$ relative humidity and using yttrium-doped TiO_2 as the electron transport layer (ETL) [101].

The n-i-p structure, or “inverted structured solar cell,” is distinguished from the p-i-n structure by the configuration of charge transport layers, as illustrated in Figure 11d. The transparent conducting substrate is positioned below the hole transporting layer (HTL) in the p-i-n configuration. Thermally depositing C-60, bathocuproine (BCP), and alone one after the other onto an ITO/PEDOT: PSS/ $\text{CH}_3\text{NH}_3\text{PbI}_3$ substrate is a typical setup for the p-i-n structure. As a result, author reported the first p-i-n perovskite solar cell with a power conversion efficiency (PCE) of 3.9%. Author grew large grains with aspect ratios of approximately 2.3–7.9, resulting in a stabilized PCE of 18.3%. Large grains formed in perovskite films as a result of Cl being added to the precursor resulted in an abnormal grain-growth behavior during a multi-cycle solution coating process. Remarkably, 18.9% was reported to be the highest PCE for p-i-n PSCs at the time of writing [102,103].

One development in solar cell technology is the creation of HTL-free PSCs. Direct Au deposition onto the perovskite layer eliminates the need for an HTL (Figure 11e), allowing the perovskite to form a heterojunction with ETL similar to TiO_2 , serving as both an absorber and a hole conductor. A PCE of 5.5% was attained by the first HTL-free PSCs [104]. Furthermore, two HTL-free cells with the following structures—ITO/ $\text{CH}_3\text{NH}_3\text{PbI}_3$ /PC 61 BM/Bis-C 60/Ag and ITO/ $\text{CH}_3\text{NH}_3\text{PbI}_3$ /C 60/BCP/Ag (BCP = 2,9-dimethyl-4,7-diphenyl-1,10-phenanthroline)—produced PCEs of 11.0% and 16.0%. BCP and Bis-C 60 were utilized in order to inhibit holes and encourage electron transport [94].

It was previously thought that TiO_2 and additional n-type semiconductors, like ETL, were required for PSC development as shown in Figure 11f. Nonetheless, Ke et al. showed that by directly forming a $\text{CH}_3\text{NH}_3\text{PbI}_{3-x}\text{Cl}_x$ film on FTO, high power conversion efficiencies (PCEs) of 14.1% could be achieved in ETL-free cells. Important characteristics were found to be uniform perovskite films with good crystallinity and the avoidance of shunting paths between HTL and FTO. Certain “ETL-free” cells showed extremely low stabilised power output [105,106], even with reasonable PCEs.

4.2. Design of Photo-Batteries

The illustration in Figure 12 reveals various methods for creating a system that combines a battery with a solar cell for charging through exposure to light. Figure 12a (photo of a rechargeable three-electrode redox flow Li-ion battery) portrays a redox-flow battery configuration with anolyte and catholyte reservoirs. When the system is exposed to light, charge separation occurs, causing electrons to reduce one species (A) while another species

oxidizes, resulting in a voltage increase of 0.7–1 V. Through discharge, electrons move through a separate circuit known as a load. On the other hand, Figure 12b (photo of a rechargeable three-electrode Li-ion battery) showcases a three-electrode photo-rechargeable battery without reservoirs. A system utilizing Si/SiO_x with Ag₆I₄WO₄ as a solid electrolyte and V₂O₅ as an intercalation material for external Ag⁺ charging was proposed by Kanbara et al. [73] in 1990. Bhattacharyya et al. [107] developed the idea of a solar rechargeable battery in 1996 by reducing hydrogen with an aqueous polysulfide anolyte using an n-CdSe semiconductor electrode. Through a different circuit connecting the anode and a third electrode, the discharge process takes place. Additionally, a two-electrode photo-battery presents another alternative, using the same circuit for both charging and discharging, similar to a standard battery, as shown in Figure 12c (photo-assisted chargeable Li-metal battery).

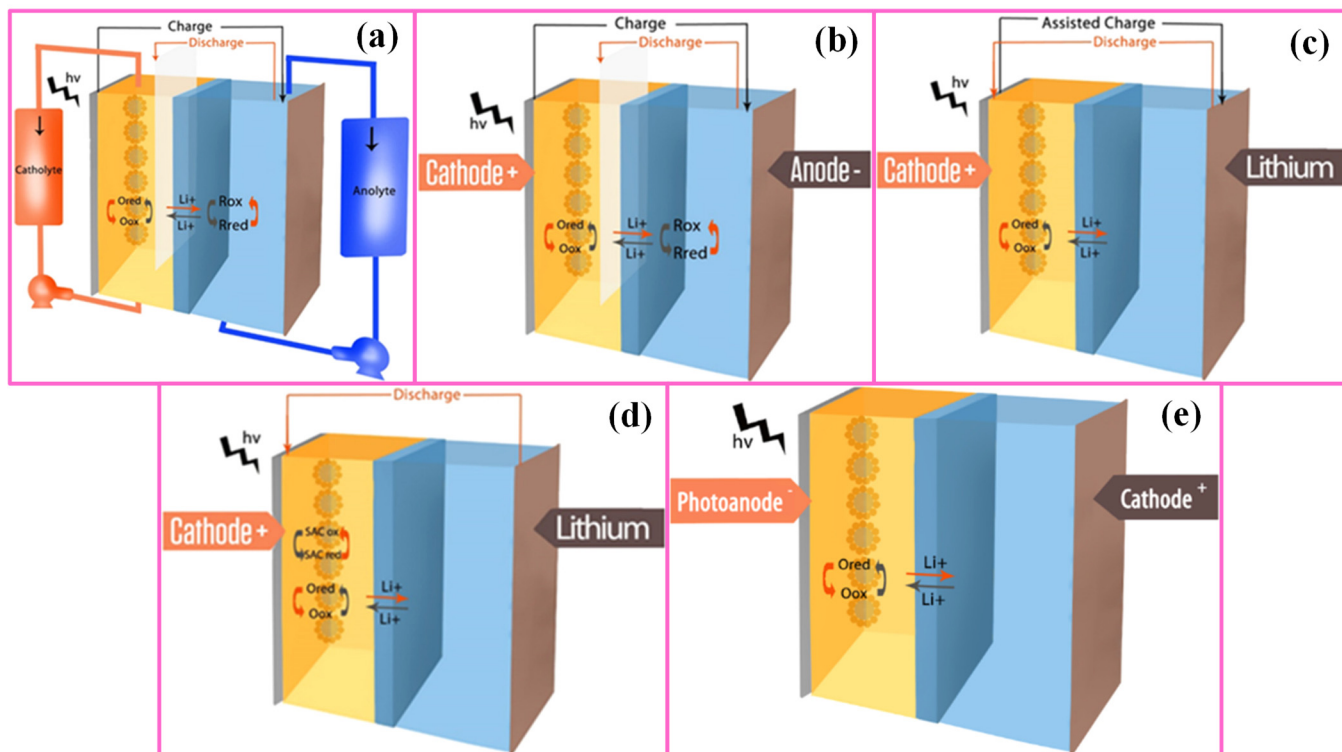


Figure 12. Design of different photo-batteries. Reproduced with permission from [86].

By modifying the semiconductor or active material's bandgap with the aid of a photo-assist, PBs have the benefit of lowering the charge voltage. A different approach uses two-electrode photo-RBs in combination with a sacrificial chemical agent (such as oxygen gas, polysulfides, or thiosulfate ions), as illustrated in Figure 12d. In this case, the photocathode is oxidized, thereby raising the battery voltage, and photoelectrons decrease a particular species. When exposed to light, no electrons pass through the external circuit, even though the battery functions normally during discharge. Using a different anode in place of metallic lithium is one alternative method, as shown in Figure 12e (photo-chargeable battery composed of a photoanode and a catholyte). Photo-Li⁺ intercalation in CuFeTe₂ was studied [74] in 1995, and photoreduction of a carbon fiber/TiO₂ composite was studied by Zou et al. [75] in 2000. In essence, the photoanode stores photoelectrons while light oxidizes the catholyte. When the battery is discharged, electrons from the external circuit can be used by a current collector to lower the catholyte. One popular method of guaranteeing a steady supply of energy is to use wiring to connect a battery to a photovoltaic (PV) system. This configuration (Figure 13a) is referred to as integration mode I and uses a four-electrode system without integration. The obvious benefits of combining these two operations, i.e., solar energy harvesting and electrochemical energy storage,

into a single device include lower costs, lower internal power losses, and smaller device volume and footprint. The three-electrode monolithic architecture, or integration mode II (Figure 13b), shares an electrode between the energy conversion and storage system. The noticeable challenge, particularly for a fully integrated two-electrode mode III device, is the discovery of an appropriate material provided that all of the above-mentioned functionalities occur at once. This advances integration to a new level. Integration mode III (Figure 13c) illustrates the highest level of integration: a two-electrode system with a single multifunctional photo-battery electrode that carries out both energy conversion (PV functionality) and storage (battery functionality) simultaneously and in the same location. Mode III has a low-polarity electrolyte to test 2-(1-cyclohexenyl)ethyl ammonium lead iodide (CHPI) stability against dissolution, Li-intercalation, and photo-assisted deintercalation (photo charging). In addition, the behavior of CHPI under illumination and contact with liquid electrolytes was evaluated.

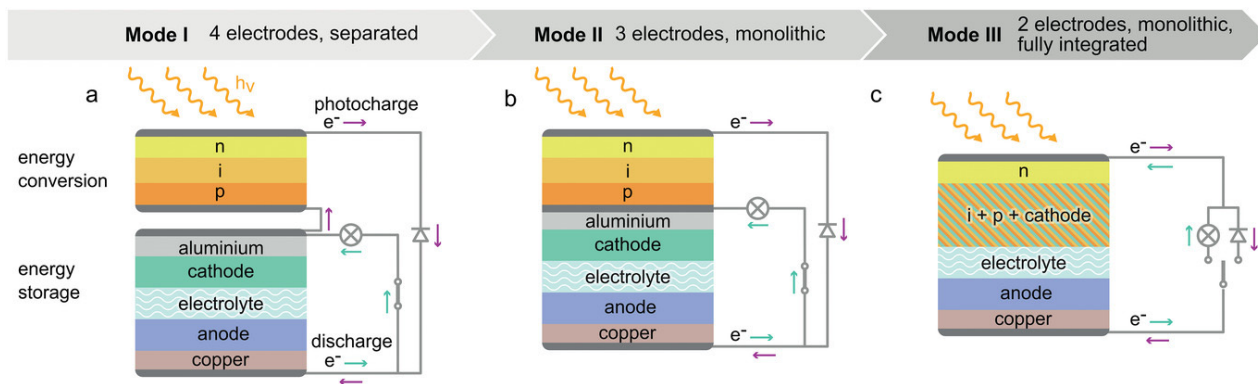


Figure 13. Diagram illustrating the various integration modes. (a) Mode I with 4 external contacts; (b) Mode II with 3 external contacts; and (c) Mode III with 2 external contacts. Reproduced with permission from [108].

5. Recent Developments in Photo-Battery Technology

For continuous and simultaneous development of photo-batteries, sustainable progress in PSCs and LIBs and their combination advancement are pivotal. PSCs have demonstrated significant enhancement in efficiency, boosting from around 3% in 2009 to over 25% today. Despite this fast-growing progress, several challenges hinder their transition into a competitive commercial technology. Four key challenges are identified from these, each presenting distinct barriers that demand specific technical and commercial targets for successful commercialization. These significant challenges are categorized as stability and durability, scalability of power conversion efficiency, manufacturability, and the validation of the technology and bankability [109].

Nevertheless, Nature's report in an interview with a solar analyst in Bloomberg NEF did not consider the present bottleneck as low efficiency. Still, it is related to both energy production by solar cells due to the lack of electrical grid infrastructure and storing excess power by batteries because of the high cost of batteries [110]. Energy storage by batteries has also improved; for example, LIBs have shown an increased volumetric energy density greater than eight times, from 55 to 450 Wh/L, from 2008 to 2020. DOE mentioned the challenges encountered in adopting energy storage, such as performance and safety, cost-competitive systems, the regulatory environment, and industry acceptance [111]. However, this hypothesis relates to large-scale energy capture. At the same time, in the small to medium scales, modifications, mostly on perovskite materials, are performed toward higher photoconversion efficiency (PCE) and capacity retention [112].

PBs, as a combined system, have been introduced as a solution to the present challenges [113]. These improvements and challenges in both PSCs and LIBs are of great importance in the developmental advancements of photo-batteries. Nevertheless, to propose enhanced performance strategies for PBs, the unique combined structure should be

considered. Low photo-electric storage-conversion efficiency plus poor cycling stability are two main drawbacks. Hence, for practical applications, reliable PBs with high power conversion efficiency and long-term stability need to be proposed [1].

5.1. Design Integration

The field of energy storage has seen a surge in design advancements recently. Li-PBs were first primarily employed in three-electrode systems, in which the battery and solar cell shared an electrode but were housed in separate compartments. Nonetheless, recent designs for 2-electrode systems have surfaced, combining energy storage and light harvesting in a single electrode. Despite having lower photoconversion and storage efficiency (PC-SE) than their three-electrode counterparts, 2-electrode Li-PBs are still very promising for commercial applications due to their lightweight, compact, and cost-effective design. Notwithstanding their potential, certain obstacles persist, such as photovoltaic efficiency and band energy alignment. On the other hand, three-electrode photovoltaic cells (PBs) exhibit superior efficiency because each cell is independent, facilitating independent optimization and mitigating the effects of light on electrolyte degradation [114].

PSC packs were unveiled in 2015 as a remedy for integrated efficiency. With a high efficiency of 7.80% for the fabricated device, a PSCs–LIB unit consisting of four single $\text{CH}_3\text{NH}_3\text{PbI}_3$ cells connected in series and a LIB cell with a LiFePO_4 cathode and $\text{Li}_4\text{Ti}_5\text{O}_{12}$ anode achieved an impressive solar-to-electric conversion rate of 12.65% (15.67% efficiency for the single cell) [1]. Despite the increasing efficiency of using packed PSCs, some researchers have proposed alternative solutions. One intriguing idea in the design process focused on the sizing of electrodes. In a particular study, the authors claimed to have achieved the highest overall efficiency of 9.9% for a solar-charged LIB with a converter, as well as a high solar-to-battery charging efficiency of 14.9%. This accomplishment was attained using an area-matched battery (large cell of 0.90 cm^2) with a PSC made of lead halide incorporating a boost converter. The authors pointed out that there are difficulties with solar-battery integration when a bigger battery (up to ten times) is coupled with a solar cell. The tested setup was too small to produce enough power for the converter to operate at maximum efficiency. For instance, four-cell PVCs (0.64 cm^2) had 13.4% solar charging efficiency [115].

Another study presented an effective method to charge a LIB without relying on multiple solar cells or complex configurations. An efficient LIB charging was achieved using a single PSC alongside an ultralow-power direct current (DC)–DC boost converter. The boost converter raised the low voltage of a single solar cell to the necessary level for complete LIB charging, incorporating maximum power point tracking and limiting the charging threshold voltage. For PSC-charged LIBs, this method produced an astounding overall efficiency of 9.36% and an average storage efficiency of 77.2% at 0.5 C discharge [116].

5.2. Chemistry Integration

Active materials have undergone the most changes for the improvement of the PBs not only toward high efficiency but also durability. In this way, various systems have been used for the storage of the harvested energy by perovskite cells depending on the application, such as zinc-ion batteries [117,118], LIBs [119,120], and SCs [121,122]. Efficiency and stability significantly lag far behind in perovskite materials, posing a crucial challenge to address before commercialization. The main cause comes from the inherent susceptibility of perovskite materials to decomposition in humid or high-temperature environments and oxidation. Various strategies are proposed to enhance long-term stability, with the most promising approach being the development of new perovskite materials resilient to the demanding conditions of solar cells. Employing suitable additives to passivate defect states in perovskite layers and enhancing device hydrophobicity, or refining the crystallographic structure through advanced preparation technologies, are known as promising ways to overcome stability challenges. For these aims, innovations in perovskite materials engineering, film engineering, carrier engineering, and photon engineering are critical

ways [123]. In addition, optimizing perovskite morphology can enhance Li-ion diffusion and overall performance. Porous structures, with increased surface area, improve intercalation affinity and reduce Li-ion diffusion length. Molecular simulations have revealed that material conductivity is strongly linked to morphology. Simple defect modifications, such as cationic disordering and doping, can substantially enhance ion intercalation by altering the material's chemical properties [117]. A 2D structure of lead bromide perovskites has proven to be highly photoactive to achieve both photocharging and Li-ion storage simultaneously. Of note, 410 mAh/g capacity was measured using this integrated 2D lead bromide system, compared to 100 mAh/g capacity for its iodide counterpart [16]. Using lead-based perovskites is one of the primary chemistry-related challenges in photovoltaics (PBs), even with their high offered capacity. Lead toxicity and poor air stability prevent PB from becoming commercially viable. Nontoxic perovskites based on germanium and tin are suggested as alternatives but are not very stable. Bismuth halide perovskite ($\text{Cs}_3\text{Bi}_2\text{I}_9$) was suggested with excellent stability, and easy deposition using solution-processing techniques at relatively low temperatures. In combination with Li metal, a PCE of ~0.43% was achieved for the first discharge of a coin-shaped cell in a combined system with a Li-ion battery [124]. Flexible systems are of considerable interest in wearable electronics and have been investigated by many other authors in an effort toward higher efficiency in photo-rechargeable systems. A flexible PSC-driven photo-rechargeable Li-ion capacitor (LIC) (with a claim by the authors as the first flexible LIC) was designed for flexible sensors. Such a module delivered 8.41% PCE and 3 V voltage at 0.1 A/g discharge current density and 6% at 1 A/g [125].

Employing Zn-ion battery systems was highlighted parallel to Li-ion storage systems. A coupled unit with an aqueous Zn battery and PSCs sandwiched in a configuration revealed an overall efficiency of 6.4% and a stable, little-degradation operation over 200 cycles. This device was reported to have a specific energy of 366 Wh/kg (at 2 A/g discharge) and a specific power of 54.01 kW/kg (at 32 A/g discharge) [119]. A quasi-solid-state (QSS) system was another proposed idea. A flexible photo-rechargeable QSS zinc-ion micro-battery was fabricated for the first time (a claim by the authors) by utilizing inkjet printing in addition to electrodeposition. A conductive Ni layer was also employed to stabilize the battery setup by overcoming galvanic corrosion in Ag/Zn layers. The excellent photovoltaic performance created a self-charging wearable electronic system. Ultrahigh VED of 148 mWh/cm³ (16.3 $\mu\text{Wh}/\text{cm}^2$), power density of 55 W/cm³ (6.1 mW/cm²) at the current density of 400 C (5 mA/cm²), and ultrafast photo-charging of 30 s were obtained [23]. A $\text{Ni}_{35}\text{Cu}_{15}\text{Zr}_{15}\text{Ti}_{35}$ metallic glass (MG) ribbon, a novel kind of multi-layered porous hybrid photoelectrode (specifically, $\text{CuxO}/\text{np-NiCu@NiCuO}/\text{MG}$, $x = 1, 2$), was created by Donghui Zheng et al. as a dealloying precursor. The photoelectrode shows a maximum specific capacitance of 1182.2 F cm^{-3} when exposed to light, which is 18% greater than when not exposed to light. Additionally, the type II $\text{In}_2\text{S}_3@\text{Bi}_2\text{S}_3$ photoelectrode demonstrated an extremely high round-trip efficiency of 96.7% when exposed to light, significantly higher than the 73% efficiency when exposed to darkness. Additionally, a limited capacity of 1000 mAh g^{-1} was achieved with a long cycle life of 1000 h at 200 mAg^{-1} [126,127]. Detailed performance strategies in perovskite photo-batteries toward enhanced PCE and cyclability and the corresponding performances are shown in Table 1.

Table 1. Enhanced performance strategies for perovskite photo-batteries toward enhanced PCE and cyclability and the corresponding performance. V_{OC} : open-circuit voltage; $\eta_{solar-to-batt}$: solar to battery charging efficiency; RGO: reduced graphene oxide; AC: activated carbon; PW: potential window.

Ref.	Enhanced Performance Strategy	Photo-Battery System		Properties		$\eta_{solar-to-batt}$ (%)	PCE (%)	Storage/Discharge Capacity (1st Cycle)	Capacity Retention (%)
		Perovskite System	Battery System	V_{OC} (V)	PW (V)				
[1]	PSC pack	4-cell PSCs	$\text{CH}_3\text{NH}_3\text{PbI}_3$	$\text{LiFePO}_4/\text{Li}_4\text{Ti}_5\text{O}_{12}$	3.84	2.5–4	12.65	7.8	140.4 mAh/g (0.5C)
		Single PSC	$\text{CH}_3\text{NH}_3\text{PbI}_3$	$\text{LiFePO}_4/\text{Li}_4\text{Ti}_5\text{O}_{12}$	0.96	1–2.6	15.67	-	-
[23]	Rear-illuminated PSC		$\text{CH}_3\text{NH}_3\text{Pb}(\text{I}_x\text{Br}_{1-x})_3$	$\text{LiCoO}_2/\text{Li}_4\text{Ti}_5\text{O}_{12}$	-	1.0–3.14	10.25	7.3	155.2 (1C) mAh/g
[117]	QSS Zn-ion system-inkjet printing-Ni layer	2-cell PSCs	$\text{Cs}_{0.05}(\text{FA}_{0.85}\text{MA}_{0.15})\text{Pb}(\text{I}_{0.85}\text{Br}_{0.15})_3$	MnO_2/Zn	1.94		16.6	-	120.0 mAh/cm (50C)
		Single PSC	$\text{Cs}_{0.05}(\text{FA}_{0.85}\text{MA}_{0.15})\text{Pb}(\text{I}_{0.85}\text{Br}_{0.15})_3$	MnO_2/Zn	1.07	1.0–1.7	11.1	5.28	184.3 mAh/cm (50C)
[116]	Different active area of PSCs	4-cell PSCs (0.64 cm ²)	$\text{CH}_3\text{NH}_3\text{PbI}_3$	$\text{LiFePO}_4/\text{Li}_4\text{Ti}_5\text{O}_{12}$	1.24	-	13.4	-	-
		PSC large (0.90 cm ²)	$\text{CH}_3\text{NH}_3\text{PbI}_3$	$\text{LiFePO}_4/\text{Li}_4\text{Ti}_5\text{O}_{12}$	1.25	-	14.9	9.8	-
[117]	Single PSC + DC–DC booster	PSC + booster	$\text{CH}_3\text{NH}_3\text{PbI}_3$	$\text{LiCoO}_2/\text{Li}_4\text{Ti}_5\text{O}_{12}$	0.96	1.0–3.14	-	9.36	151.3 mAh/g (0.1C)
		Single PSC	$\text{CH}_3\text{NH}_3\text{PbI}_3$	$\text{LiCoO}_2\text{-Li}_4\text{Ti}_5\text{O}_{12}$	0.68	1.0–3.14	14.2	7.89	88 (10 cycles) 81 (20 cycles)
[125]	Lead-free perovskite coin-cell format		$\text{Cs}_3\text{Bi}_2\text{I}_9$	Li metal	-	0.01–2.50	-	~0.43	410 mAh/g
[16]	Perovskite coin-cell format	3D iodide	$(\text{C}_6\text{H}_9\text{C}_2\text{H}_4\text{NH}_3)_2\text{PbBr}_4$	Li metal	-	1.4–3	-	0.034	90–100 mAh/g
		2D bromide	$(\text{C}_6\text{H}_9\text{C}_2\text{H}_4\text{NH}_3)_2\text{PbI}_4$	Li metal	-	1.4–3	-	0.034	410 mAh/g
[121]	Zn-ion system		$\text{Cs}_{0.15}\text{FA}_{0.85}\text{PbI}_3$	$\text{Co}_2\text{P-CoP-NiCoO}_2/\text{Zn}$	-	1.4–1.9	-	6.4	170 mAh/g
									No fading (200 cycles)

6. Conclusions

This review culminates in discussing the current landscape and prospects for developing perovskite-based photo-RBs. While the integration of PSCs with SCs and the advancements in IPSs have demonstrated significant potential, there are still numerous challenges to overcome, particularly in terms of device stability, energy efficiency, and cost-effectiveness. The review identifies the need for further research into optimizing material properties and device architectures to enhance the performance and durability of these batteries. Future directions also include exploring new material combinations and innovative fabrication techniques that could pave the way for the next generation of energy storage systems. Perovskite-based solar cells are a promising technology for renewable energy but face several challenges that need to be addressed to improve their practical application. These challenges include low energy-storage efficiency, high energy losses, poor environmental and thermal stability, environmental toxicity, a lack of standardized testing protocols, the tendency for electrolyte leakage, issues with material compatibility, and difficulties with encapsulation and packaging that are important for commercialization. The future direction to overcome these challenges lies in several key areas. Integration of tandem PSCs with SCs, selection of compatible materials, and the right choice of electrolytes is crucial. Ensuring long-term stability and the development of lead-free, high-efficiency PSCs are also important goals. Further engineering efforts are required for integration configuration and improvements in the electrodes and substrates used in SCs. Addressing these areas will pave the way for future commercialization, potentially leading to more efficient, stable, and environmentally friendly solar energy solutions.

Author Contributions: A.K.M.R. wrote the review manuscript and produced the graphics. A.N., M.D.B., D.M. and K.Z. designed the structure of the review, collected the papers related to the topic of the review, and completed the language corrections, with all authors contributing equally. All authors have read and agreed to the published version of the manuscript.

Funding: This research was funded Concordia University.

Acknowledgments: This research was funded by Concordia University and Volt-Age; we extend our deepest gratitude to Concordia University and Volt-Age for support. <https://www.concordia.ca/research/volt-age.html>.

Conflicts of Interest: The authors declare no conflicts of interest.

References

1. Xu, J.; Chen, Y.; Dai, L. Efficiently photo-charging Li-ion battery by perovskite solar cell. *Nat. Commun.* **2015**, *6*, 8103. [[CrossRef](#)]
2. Tewari, N.; Lam, D.; Li, C.H.A.; Jonathan, E. Halper Recent advancements in batteries and photo-batteries using metal halide perovskites. *APL Mater.* **2022**, *10*, e040905. [[CrossRef](#)]
3. Haight, R.; Haensch, W.; Friedman, D. Solar-powering the Internet of Things. *Science* **2016**, *353*, 124–125. [[CrossRef](#)] [[PubMed](#)]
4. Ahmad, S.; Copic, D.; George, C.; De Volder, M. Hierarchical assemblies of carbon nanotubes for ultraflexible Li-ion batteries. *Adv. Mater.* **2016**, *28*, 6705–6710. [[CrossRef](#)]
5. Chen, J.; Huang, Y.; Zhang, N.; Zou, H.; Liu, R.; Tao, C.; Fan, X.; Wang, Z.L. Micro-cable structured textile for simultaneously harvesting solar and mechanical energy. *Nat. Energy* **2016**, *1*, 16138. [[CrossRef](#)]
6. Zhou, G.; Li, F.; Cheng, H.-M. Progress in flexible lithium batteries and future prospects. *Energy Environ. Sci.* **2014**, *7*, 1307–1338. [[CrossRef](#)]
7. Zhou, G.; Sun, J.; Jin, Y.; Chen, W.; Zu, C.; Zhang, R.; Qiu, Y.; Zhao, J.; Zhuo, D.; Liu, Y.; et al. Sulfophilic nickel phosphosulfide enabled Li₂S impregnation in 3D graphene cages for Li-S batteries. *Adv. Mater.* **2017**, *29*, 1603366. [[CrossRef](#)] [[PubMed](#)]
8. Zhang, N.; Chen, J.; Huang, Y.; Guo, W.; Yang, J.; Du, J.; Fan, X.; Tao, C. A Wearable All-Solid Photovoltaic Textile. *Adv. Mater.* **2016**, *28*, 263–269. [[CrossRef](#)]
9. Vlad, A.; Singh, N.; Galande, C.; Ajayan, P.M. Design considerations for unconventional electrochemical energy storage architectures. *Adv. Energy Mater.* **2015**, *5*, 1402115. [[CrossRef](#)]
10. Xu, J.; Wu, H.; Lu, L.; Leung, S.-F.; Chen, D.; Chen, X.; Fan, Z.; Shen, G.; Li, D. Integrated photo-supercapacitor based on bi-polar TiO₂ nanotube arrays with selective one-side plasma-assisted hydrogenation. *Adv. Funct. Mater.* **2014**, *24*, 1840–1846. [[CrossRef](#)]
11. Méndez, M.A.; Peljo, P.; Scanlon, M.D.; Vrubel, H.; Girault, H.H. Photo-ionic cells: Two solutions to store solar energy and generate electricity on demand. *J. Phys. Chem. C* **2014**, *118*, 16872–16883. [[CrossRef](#)]

12. Miyasaka, T.; Ikeda, N.; Murakami, T.N.; Teshima, K. Light energy conversion and storage with soft carbonaceous materials that solidify mesoscopic electrochemical interfaces. *Chem. Lett.* **2007**, *36*, 480–487. [[CrossRef](#)]
13. Thimmappa, R.; Paswan, B.; Gaikwad, P.; Devendrachari, M.C.; Makri Nimbegondi Kotresh, H.; Rani Mohan, R.; Pattayil Alias, J.; Thotiyil, M.O. Chemically chargeable photo battery. *J. Phys. Chem. C* **2015**, *119*, 14010–14016. [[CrossRef](#)]
14. Paolella, A.; Faure, C.; Bertoni, G.; Marras, S.; Guerfi, A.; Darwiche, A.; Hovington, P.; Commarieu, B.; Wang, Z.; Prato, M.; et al. Light-assisted delithiation of lithium iron phosphate nanocrystals towards photo-rechargeable lithium ion batteries. *Nat. Commun.* **2017**, *8*, 14643. [[CrossRef](#)] [[PubMed](#)]
15. Nguyen, O.; Courtin, E.; Sauvage, F.; Krins, N.; Sanchez, C.; Laberty-Robert, C. Shedding light on the light-driven Li-ion de-insertion reaction: Towards the design of a photo-rechargeable battery. *J. Mater. Chem. A* **2017**, *5*, 5927–5933. [[CrossRef](#)]
16. Ahmad, S.; George, C.; Beesley, D.J.; Baumberg, J.J.; De Volder, M. Photo-Rechargeable Organo-Halide Perovskite Batteries. *Nano Lett.* **2018**, *18*, 1856–1862. [[CrossRef](#)]
17. Armaroli, N.; Balzani, V. Towards an electricity-powered world. *Energy Environ. Sci.* **2011**, *4*, 3193–3222. [[CrossRef](#)]
18. Weinstein, L.A.; Loomis, J.; Bhatia, B.; Bierman, D.M.; Wang, E.N.; Chen, G. Concentrating solar power. *Chem. Rev.* **2015**, *115*, 12797–12838. [[CrossRef](#)]
19. Kruitwagen, L.; Story, K.T.; Friedrich, J.; Byers, L.; Skillman, S.; Hepburn, C. A global inventory of solar photovoltaic generating units-dataset. *Nature* **2021**, *598*, 604–611. [[CrossRef](#)]
20. Um, H.D.; Choi, K.H.; Hwang, I.; Kim, S.H.; Seo, K.; Lee, S.Y. Monolithically integrated, photo-rechargeable portable power sources based on miniaturized Si solar cells and printed solid-state LIBs. *Energy Environ. Sci.* **2017**, *10*, 931–940. [[CrossRef](#)]
21. Zeng, Q.; Lai, Y.; Jiang, L.; Liu, F.; Hao, X.; Wang, L.; Green, M.A. Integrated photorechargeable energy storage system: Next-generation power source driving the future. *Adv. Energy Mater.* **2020**, *10*, 1903930. [[CrossRef](#)]
22. Zhang, X.; Song, W.L.; Tu, J.; Wang, M.; Jiao, S. A review of integrated systems based on PSCs and energy storage units: Fundamental, progresses, challenges, and perspectives. *Adv. Sci.* **2021**, *8*, 2100552. [[CrossRef](#)] [[PubMed](#)]
23. Gurung, A.; Reza, K.M.; Mabrouk, S.; Bahrami, B.; Pathak, R.; Lamsal, B.S.; Rahman, S.I.; Ghimire, N.; Bobba, R.S.; Chen, K.; et al. Rear-Illuminated Perovskite Photorechargeable Lithium Battery. *Adv. Funct. Mater.* **2020**, *30*, 2001865. [[CrossRef](#)]
24. Hodes, G.; Manassen, J.; Cahen, D. Photoelectrochemical energy conversion and storage using polycrystalline chalcogenide electrodes. *Nature* **1976**, *261*, 403–404. [[CrossRef](#)]
25. Lv, J.; Tan, Y.X.; Xie, J.; Yang, R.; Yu, M.; Sun, S.; Li, M.; Yuan, D.; Wang, Y. Direct solar-to-electrochemical energy storage in a functionalized covalent organic framework. *Angew. Chem.* **2018**, *130*, 12898–12902. [[CrossRef](#)]
26. Chen, P.; Li, G.R.; Li, T.T.; Gao, X.P. Solar-driven rechargeable lithium–sulfur battery. *Adv. Sci.* **2019**, *6*, 1900620. [[CrossRef](#)] [[PubMed](#)]
27. Li, N.; Wang, Y.; Tang, D.; Zhou, H. Integrating a photocatalyst into a hybrid lithium–sulfur battery for direct storage of solar energy. *Angew. Chem. Int. Ed.* **2015**, *54*, 9271–9274. [[CrossRef](#)]
28. Liu, Y.; Li, N.; Wu, S.; Liao, K.; Zhu, K.; Yi, J.; Zhou, H. Reducing the charging voltage of a Li–O₂ battery to 1.9 V by incorporating a photocatalyst. *Energy Environ. Sci.* **2015**, *8*, 2664–2667.
29. Yang, X.Y.; Feng, X.L.; Jin, X.; Shao, M.Z.; Yan, B.L.; Yan, J.M.; Zhang, X.B. An Illumination-Assisted Flexible Self-Powered Energy System Based on a Li–O₂ Battery. *Angew. Chem.* **2019**, *131*, 16563–16567. [[CrossRef](#)]
30. Liu, X.; Yuan, Y.; Liu, J.; Liu, B.; Chen, X.; Ding, J.; Hu, W. Utilizing solar energy to improve the oxygen evolution reaction kinetics in zinc–air battery. *Nat. Commun.* **2019**, *10*, 4767. [[CrossRef](#)]
31. Ingavale, S.; Gopalakrishnan, M.; Enoch, C.M.; Pornrungroj, C.; Rittirua, M.; Praserthdam, S.; Kheawhom, S. Strategic Design and Insights into Lanthanum and Strontium Perovskite Oxides for Oxygen Reduction and Oxygen Evolution Reactions. *Small* **2024**, *20*, 2308443. [[CrossRef](#)] [[PubMed](#)]
32. Zhao, C.; Zhang, X.; Yu, M.; Wang, A.; Wang, L.; Xue, L.; Wang, W. Cooperative Catalysis toward Oxygen Reduction Reaction under Dual Coordination Environments on Intrinsic AMnO₃-Type Perovskites via Regulating Stacking Configurations of Coordination Units. *Adv. Mater.* **2020**, *32*, 2006145. [[CrossRef](#)]
33. Gholamrezaei, S.; Salavati-Niasari, M. Sonochemical synthesis of SrMnO₃ nanoparticles as an efficient and new catalyst for O₂ evolution from water splitting reaction. *Ultrason. Sonochem.* **2018**, *40*, 651–663. [[CrossRef](#)]
34. Choi, S.R.; So, I.S.; Lee, S.W.; Yoo, J.; Seo, Y.S.; Cho, H.S.; Park, J.Y. 3D architecture double perovskite NdBa_{0.5}Sr_{0.5}Co_{1.5}Fe_{0.5}O_{5+δ} embedded hollow-net Co₃O₄ bifunctional electrocatalysts coupled with N-doped CNT and reduced graphene oxide for oxygen electrode reactions. *J. Alloys Compd.* **2020**, *823*, 153782. [[CrossRef](#)]
35. Bochu, B.; Chenavas, J.; Joubert, J.C.; Marezio, M. High pressure synthesis and crystal structure of a new series of perovskite-like compounds CMn₇O₁₂ (C = Na, Ca, Cd, Sr, La, Nd). *J. Solid State Chem.* **1974**, *11*, 88–93. [[CrossRef](#)]
36. Long, Y. A-site ordered quadruple perovskite oxides. *Chin. Phys. B* **2016**, *25*, e078108. [[CrossRef](#)]
37. Yamada, I.; Fujii, H.; Takamatsu, A.; Ikeno, H.; Wada, K.; Tsukasaki, H.; Yagi, S. Bifunctional oxygen reaction catalysis of quadruple manganese perovskites. *Adv. Mater.* **2017**, *29*, 1603004. [[CrossRef](#)]
38. Shigematsu, K.; Shimizu, K.; Yamamoto, K.; Nishikubo, T.; Sakai, Y.; Nikolaev, S.A.; Das, H.; Azuma, M. Strain Manipulation of Magnetic Anisotropy in Room-Temperature Ferrimagnetic Quadruple Perovskite CeCu₃Mn₄O₁₂. *ACS Appl. Electron. Mater.* **2019**, *1*, 2514–2521. [[CrossRef](#)]
39. Aftab, S.; Li, X.; Kabir, F.; Akman, E.; Aslam, M.; Pallavolu, M.R.; Kooyyada, G.; Mohammed, A.; Assiri, M.A.; Rajpar, A.H. Lighting the future: Perovskite nanorods and their advances across applications. *Nano Energy* **2024**, *124*, 109504. [[CrossRef](#)]

40. Gao, L.; Wang, X.; Ye, X.; Wang, W.; Liu, Z.; Qin, S.; Long, Y. Near-room-temperature ferrimagnetic ordering in a B-site-disordered 3d–5d-hybridized quadruple perovskite oxide, $\text{CaCu}_3\text{Mn}_2\text{Os}_2\text{O}_{12}$. *Inorg. Chem.* **2019**, *58*, 15529–15535. [[CrossRef](#)]
41. Li, S.F.; Zhang, B.Q.; Li, Y.N.; Yan, D. Regulating the Electronic Structure of Ruddlesden–Popper-Type Perovskite by Chlorine Doping for Enhanced Oxygen Evolution Activity. *Inorg. Chem.* **2023**, *62*, 11233–11239. [[CrossRef](#)] [[PubMed](#)]
42. IR de Larramendi, N.; Ortiz-Vitoriano, I.B.; Dzul-Bautista, T. Rojo, in *Perovskite Materials—Synthesis, Characterisation, Properties, and Applications*; Pan, L., Zhu, G., Eds.; InTechOpen: London, UK, 2016; pp. 589–617.
43. Fop, S.; McCombie, K.S.; Wildman, E.J.; Skakle, J.M.; McLaughlin, A.C. Hexagonal perovskite derivatives: A new direction in the design of oxide ion conducting materials. *Chem. Commun.* **2019**, *55*, 2127–2137. [[CrossRef](#)] [[PubMed](#)]
44. Chen, C.F.; King, G.; Dickerson, R.M.; Papin, P.A.; Gupta, S.; Kellogg, W.R.; Wu, G. Oxygen-deficient BaTiO_{3-x} perovskite as an efficient bifunctional oxygen electrocatalyst. *Nano Energy* **2015**, *13*, 423–432. [[CrossRef](#)]
45. Gobeng, R.; Monama, A.B.; Kabelo, E.; Ramohlola, A.; Emmanuel, I.; Iwuoha, B.; Kwena, D.; Modibane, A. Progress on perovskite materials for energy application. *Results Chem.* **2022**, *4*, 100321. [[CrossRef](#)]
46. DSchmidt, S.; Hager, M.D.; Schubert, U.S. Photo-Rechargeable electric energy storage systems. *Adv. Energy Mater.* **2016**, *6*, 1500369. [[CrossRef](#)]
47. Julien, C.; Nazri, G.A. *Solid State Batteries: Materials Design and Optimization*; Kluwer: Boston, MA, USA, 1994.
48. Jasinski, R. *High-Energy Batteries*; Plenum: New York, NY, USA, 1967.
49. Julien, C. Design considerations for lithium batteries. In *Materials for LIBs*; Julien, C., Stoyanov, Z., Eds.; Kluwer: Dordrecht, The Netherlands, 2000; pp. 1–20.
50. Bouguern, M.D.; Madikere Raghunatha Reddy, A.K.; Li, X.; Deng, S.; Laryea, H.; Zaghib, K. Engineering Dry Electrode Manufacturing for Sustainable LIBs. *Batteries* **2024**, *10*, 39. [[CrossRef](#)]
51. Yoshio, M.; Brodd, R.J.; Kozawa, A. *Lithium Batteries, Science and Technologies*; Springer: New York, NY, USA, 2009.
52. Julien, C.; Mauger, A.; Vijh, A.; Zaghib, K. Lithium Batteries: Science and Technology. *MRS Bull.* **2016**, *41*, 707. [[CrossRef](#)]
53. Pandolfo, A.G.; Hollenkamp, A.F. Carbon properties and their role in SCs. *J. Power Sources* **2006**, *157*, 11–27. [[CrossRef](#)]
54. Kötz, R.; Carlen, M.J.E.A. Principles and applications of electrochemical capacitors. *Electrochim. Acta* **2000**, *45*, 2483–2498. [[CrossRef](#)]
55. Miller, J.R.; Simon, P. Electrochemical capacitors for energy management. *Science* **2008**, *321*, 651–652. [[CrossRef](#)]
56. González, A.; Goikolea, E.; Barrena, J.A.; Mysyk, R. Review on SCs: Technologies and materials. *Renew. Sustain. Energy Rev.* **2016**, *58*, 1189–1206. [[CrossRef](#)]
57. Tehrani, Z.; Thomas, D.J.; Korochkina, T.; Phillips, C.O.; Lupo, D.; Lehtimäki, S.; Gethin, D.T. Large-area printed supercapacitor technology for low-cost domestic green energy storage. *Energy* **2017**, *118*, 1313–1321. [[CrossRef](#)]
58. Zhang, L.L.; Zhao, X.S. Carbon-based materials as supercapacitor electrodes. *Chem. Soc. Rev.* **2009**, *38*, 2520–2531. [[CrossRef](#)] [[PubMed](#)]
59. Ahammad, A.S.; Odhikari, N.; Shah, S.S.; Hasan, M.M.; Islam, T.; Pal, P.R.; Qasem, M.A.A.; Aziz, M.A. Porous tal palm carbon nanosheets: Preparation, characterization and application for the simultaneous determination of dopamine and uric acid. *Nanoscale Adv.* **2019**, *1*, 613–626. [[CrossRef](#)] [[PubMed](#)]
60. Shah, S.S.; Qasem, M.A.A.; Berni, R.; Del Casino, C.; Cai, G.; Contal, S.; Ahmad, I.; Siddiqui, K.S.; Gatti, E.; Predieri, S.; et al. Physico-chemical properties and toxicological effects on plant and algal models of carbon nanosheets from a nettle fibre clone. *Sci. Rep.* **2021**, *11*, 6945. [[CrossRef](#)] [[PubMed](#)]
61. Song, Q.; Chen, J.; Chen, J.; Chen, G. Completely decentralized energy management system for fuel cell-battery-ultracapacitor hybrid energy storage system. *IEEE Trans. Ind. Electron.* **2023**, *13*, 428–449. [[CrossRef](#)]
62. Mineo, G.; Bruno, E.; Mirabella, S. Advances in WO_3 -Based Supercapacitors: State-of-the-Art Research and Future Perspectives. *Nanomaterials* **2023**, *13*, 1418. [[CrossRef](#)] [[PubMed](#)]
63. Ates, M.; Chebil, A.; Yoruk, O.; Dridi, C.; Turkyilmaz, M. Reliability of electrode materials for SCs and batteries in energy storage applications: A review. *Ionics* **2022**, *28*, 27–52. [[CrossRef](#)]
64. Singha, D.K.; Mohanty, R.I.; Bhanja, P.; Jena, B.K. Metal–organic framework and graphene composites: Advanced materials for electrochemical supercapacitor applications. *Mater. Adv.* **2023**, *4*, 4679–4706. [[CrossRef](#)]
65. Liu, L.; Niu, Z.; Chen, J. Unconventional SCs from nanocarbon-based electrode materials to device configurations. *Chem. Soc. Rev.* **2016**, *45*, 4340–4363. [[CrossRef](#)]
66. Sharma, P.; Bhatti, T.S. A review on electrochemical double-layer capacitors. *Energy Convers. Manag.* **2010**, *51*, 2901–2912. [[CrossRef](#)]
67. Bai, Y.; Liu, C.; Chen, T.; Li, W.; Zheng, S.; Pi, Y.; Luo, Y.; Pang, H. MXene-copper/cobalt hybrids via lewis acidic molten salts etching for high performance symmetric SCs. *Angew. Chem.* **2021**, *133*, 25522–25526. [[CrossRef](#)]
68. Ke, Q.; Wang, J. Graphene-based materials for supercapacitor electrodes—A review. *J. Mater.* **2016**, *2*, 37–54. [[CrossRef](#)]
69. Shi, W.; Zhu, J.; Sim, D.H.; Tay, Y.Y.; Lu, Z.; Zhang, X.; Sharma, Y.; Srinivasan, M.; Zhang, H.; Hng, H.H.; et al. Achieving high specific charge capacitances in Fe_3O_4 /reduced graphene oxide nanocomposites. *J. Mater. Chem.* **2011**, *21*, 3422–3427. [[CrossRef](#)]
70. Hada, H.; Takaoka, K.; Saikawa, M.; Yonezawa, Y. Energy Conversion and Storage in Solid-state Photogalvanic Cells. *Bull. Chem. Soc. Jpn.* **1981**, *54*, 1640–1644. [[CrossRef](#)]
71. Yonezawa, Y.; Okai, M.; Ishino, M.; Hada, H. Photochemical Storage Battery with an n-GaP Photoelectrode. *Bull. Chem. Soc. Jpn.* **1983**, *56*, 2873–2876. [[CrossRef](#)]

72. Betz, G.; Fiechter, S.; Tributsch, H. Photon Energy Conversion and Storage with a Light-driven Insertion Reaction. *J. Appl. Phys.* **1987**, *62*, 4597–4605. [CrossRef]
73. Kanbara, T.; Takada, K.; Yamamura, Y.; Kondo, S. Photo-Rechargeable Solid-State Battery. *Solid State Ion.* **1990**, *40–41*, 955–958. [CrossRef]
74. Nomiyama, T.; Kuriyaki, H.; Hirakawa, K. Photo-Rechargeable Battery Using New Layer Compound CuFeTe₂. *Synth. Met.* **1995**, *71*, 2237–2238. [CrossRef]
75. Zou, X.; Maesako, N.; Nomiyama, T.; Horie, Y.; Miyazaki, T. Photo-Rechargeable Battery with TiO₂/Carbon Fiber Electrodes Prepared by Laser Deposition. *Sol. Energy Mater. Sol. Cells* **2000**, *62*, 133–142. [CrossRef]
76. Hauch, A.; Georg, A.; Krasovec, U.O.; Orel, B. Photovoltaically Self-Charging Battery. *J. Electrochem. Soc.* **2002**, *149*, A1208. [CrossRef]
77. Al-Ezzi, A.S.; Ansari, M.N.M. Photovoltaic Solar Cells: A Review. *Appl. Syst. Innov.* **2022**, *5*, 67. [CrossRef]
78. Floyd, T.L. *Electronic Devices*, 9th ed.; Pearson: London, UK, 2011.
79. Julien, C.; Mauger, A.; Vijh, A.; Zaghib, K. Lithium Batteries. In *Lithium Batteries*; Springer: Cham, Switzerland, 2016. [CrossRef]
80. Dahbi, M.; Ghamous, F.; Tran-Van, F.; Lemordant, D.; Anouti, M. Comparative study of EC/DMC LiTFSI and LiPF₆ electrolytes for electrochemical storage. *J. Power Sources* **2011**, *196*, 9743–9750. [CrossRef]
81. Zaghib, K.; Guerfi, A.; Hovington, P.; Vijh, A.; Trudeau, M.; Mauger, A.; Goodenough, J.B.; Julien, C.M. Review and analysis of nanostructured olivine-based lithium RBs: Status and trends. *J. Power Sources* **2013**, *232*, 357–369. [CrossRef]
82. Zaghib, K.; Dontigny, M.; Guerfi, A.; Charest, P.; Rodrigues, I.; Mauger, A.; Julien, C.M. Safe and fast-charging Li-ion battery with long shelf life for power applications. *J. Power Sources* **2011**, *196*, 3949–3954. [CrossRef]
83. Milot, R.L.; Sutton, R.J.; Eperon, G.E.; Haghhighirad, A.A.; Martinez Hardigree, J.; Miranda, L.; Snaith, H.J.; Johnston, M.B.; Herz, L.M. Charge-carrier dynamics in 2D hybrid metal-halide perovskites. *Nano Lett.* **2016**, *16*, 7001–7007. [CrossRef] [PubMed]
84. Paolella, A.; Vijh, A.; Guerfi, A.; Zaghib, K.; Faure, C. Review—Li-Ion Photo-Batteries: Challenges and Opportunities. *J. Electrochem. Soc.* **2020**, *167*, 120545. [CrossRef]
85. Zhang, C. Solar storage: Two-electrode single systems. *Nat. Energy* **2017**, *2*, 17079. [CrossRef]
86. Yu, M.; Ren, X.; Ma, L.; Wu, Y. Integrating a redox-coupled dye-sensitized photoelectrode into a lithium-oxygen battery for photoassisted charging. *Nat. Commun.* **2014**, *5*, 5111. [CrossRef]
87. Li, Q.; Li, N.; Ishida, M.; Zhou, H. Saving electric energy by integrating a photoelectrode into a Li-ion battery. *J. Mater. Chem. A* **2015**, *3*, 20903. [CrossRef]
88. Wang, Z.; Chiu, H.; Paolella, A.; Zaghib, K.; Demopoulos, G.P. Lithium photo-intercalation of CdS-Sensitized WO₃ anode for energy storage and photoelectrochromic applications. *ChemSusChem* **2019**, *12*, 2220–2230. [CrossRef] [PubMed]
89. Dokouzis, A.; Bella, F.; Theodosiou, K.; Gerbaldi, C.; Leftheriotis, G. Photoelectrochromic devices with cobalt redox electrolytes. *Mater. Today Energy* **2020**, *15*, 100365. [CrossRef]
90. Maloney, J. *From Mineral Exploration to Advanced Manufacturing: Developing Value Chains for Critical Minerals in Canada*; RNNR Committee Report; Parliament of Canada: Ottawa, ON, Canada, 2021.
91. Critical Minerals Data Explorer. Available online: <https://www.iea.org/data-and-statistics/data-tools/critical-minerals-data-explorer> (accessed on 17 May 2024).
92. IEA. *Critical Minerals Market Review 2023*; International Energy Agency (IEA): Paris, France, 2023.
93. Oyewole, O.K.; Oyelade, O.V.; Ichwani, R.; Koech, R.; Oyewole, D.O.; Cromwell, J.; Olanrewaju, Y.; Soboyejo, W.O. *Mechanical Properties of Solar Cell Structures, Comprehensive Structural Integrity*, 2nd ed.; Elsevier: Amsterdam, The Netherlands, 2023; pp. 185–208. ISBN 9780323919456. [CrossRef]
94. Zuo, C.; Henk; Bolink, J.; Han, H.; Huang, J.; Cahen, D.; Ding, L. Advances in PSCs. *Adv. Sci.* **2016**, *3*, 1500324. [CrossRef] [PubMed]
95. Kojima, A.; Teshima, K.; Miyasaka, T.; Shirai, Y. Novel Photoelectrochemical Cell with Mesoscopic Electrodes Sensitized by Lead-Halide Compounds (2). In Proceedings of the 210th ECS Meeting, Cancun, Mexico, 30 June 2006.
96. Kojima, A.; Teshima, K.; Shirai, Y.; Miyasaka, T. Organometal halide perovskites as visible-light sensitizers for photovoltaic cells. *J. Am. Chem. Soc.* **2009**, *131*, 6050–6051. [CrossRef] [PubMed]
97. Im, J.H.; Lee, C.R.; Lee, J.W.; Park, S.W.; Park, N.G. 6.5% efficient perovskite quantum-dot-sensitized solar cell. *Nanoscale* **2011**, *3*, 4088–4093. [CrossRef] [PubMed]
98. Kim, H.S.; Lee, C.R.; Im, J.H.; Lee, K.B.; Moehl, T.; Marchioro, A.; Moon, S.J.; Humphry-Baker, R.; Yum, J.H.; Moser, J.E.; et al. Lead iodide perovskite sensitized all-solid-state submicron thin film mesoscopic solar cell with efficiency exceeding 9%. *Sci. Rep.* **2012**, *2*, 591. [CrossRef] [PubMed]
99. Yang, W.S.; Noh, J.H.; Jeon, N.J.; Kim, Y.C.; Ryu, S.; Seo, J.; Seok, S.I. High-performance photovoltaic perovskite layers fabricated through intramolecular exchange. *Science* **2015**, *348*, 1234–1237. [CrossRef] [PubMed]
100. Ball, J.M.; Lee, M.M.; Hey, A.; Snaith, H.J. Low-temperature processed meso-superstructured to thin-film PSCs. *Energy Environ. Sci.* **2013**, *6*, 1739–1743. [CrossRef]
101. Zhou, H.; Chen, Q.; Li, G.; Luo, S.; Song, T.B.; Duan, H.S.; Hong, Z.; You, J.; Liu, Y.; Yang, Y. Interface engineering of highly efficient PSCs. *Science* **2014**, *345*, 542–546. [CrossRef]
102. Bi, C.; Wang, Q.; Shao, Y.; Yuan, Y.; Xiao, Z.; Huang, J. Non-wetting surface-driven high-aspect-ratio crystalline grain growth for efficient hybrid PSCs. *Nat. Commun.* **2015**, *6*, 7747. [CrossRef]

103. Dong, Q.; Yuan, Y.; Shao, Y.; Fang, Y.; Wang, Q.; Huang, J. Abnormal crystal growth in $\text{CH}_3\text{NH}_3\text{PbI}_{3-x}\text{Cl}_x$ using a multi-cycle solution coating process. *Energy Environ. Sci.* **2015**, *8*, 2464–2470. [CrossRef]
104. Etgar, L.; Gao, P.; Xue, Z.; Peng, Q.; Chandiran, A.K.; Liu, B.; Nazeeruddin, M.K.; Gratzel, M. Mesoscopic $\text{CH}_3\text{NH}_3\text{PbI}_3/\text{TiO}_2$ heterojunction solar cells. *J. Am. Chem. Soc.* **2012**, *134*, 17396–17399. [CrossRef]
105. Ke, W.; Fang, G.; Wan, J.; Tao, H.; Liu, Q.; Xiong, L.; Qin, P.; Wang, J.; Lei, H.; Yang, G.; et al. Efficient hole-blocking layer-free planar halide perovskite thin-film solar cells. *Nat. Commun.* **2015**, *6*, 6700. [CrossRef] [PubMed]
106. Zhang, Y.; Liu, M.; Eperon, G.E.; Leijtens, T.C.; McMeekin, D.; Saliba, M.; Zhang, W.; de Bastiani, M.; Petrozzi, A.; Herz, L.M.; et al. Charge selective contacts, mobile ions and anomalous hysteresis in organic-inorganic PSCs. *Mater. Horiz.* **2015**, *2*, 315–322. [CrossRef]
107. Bhattacharyya, R.G.; Mandal, D.P.; Bera, S.C.K.K. Rohatgi-Mukherjee, Photo electro synthesis of Dihydrogen via water-splitting using $\text{S}(2-x)$ as ana anolyte: A first step for a viable solar rechargeable battery. *Int. J. Hydrogen Energy* **1996**, *21*, 343–347. [CrossRef]
108. Büttner, J.; Berestok, T.; Burger, S.; Schmitt, M.; Daub, M.; Hillebrecht, H.; Krossing, I.; Fischer, A. Are Halide-Perovskites Suitable Materials for Battery and Solar-Battery Applications—Fundamental Reconsiderations on Solubility, Lithium Intercalation, and Photo-Corrosion. *Adv. Funct. Mater.* **2022**, *32*, 2206958. [CrossRef]
109. PSCs. *Solar Energy Technologies Office*; The US Department of Energy (DOE): SW Washington, DC, USA, 2023.
110. Peplow, M. A new kind of solar cell is coming: Is it the future of green energy? *Nature* **2023**, *623*, 902–905. [CrossRef]
111. Volumetric Energy Density of LIBs Increased by More Than Eight Times between 2008 and 2020. Available online: <https://www.energy.gov/eere/vehicles/articles/fotw-1234-april-18-2022-volumetric-energy-density-Li-ion-batteries> (accessed on 18 April 2022).
112. US Department of Energy. *Spotlight: Solving Industry's Energy Storage Challenges*; Office of Technology Transfer: SW Washington, DC, USA, 2019. Available online: <https://www.energy.gov/sites/prod/files/2019/07/f64/2018-OTT-Energy-Storage-Spotlight.pdf> (accessed on 5 August 2024).
113. Pujari, A.; Kim, B.-M.; Sayed, F.N.; Sanders, K.; Dose, W.M.; Mathieson, A.; Grey, C.P.; Greenham, N.C.; De Volder, M. Does Heat Play a Role in the Observed Behavior of Aqueous Photobatteries? *ACS Energy Lett.* **2023**, *8*, 4625–4633. [CrossRef] [PubMed]
114. Salunke, A.D.; Chamola, S.; Mathieson, A.; Boruah, B.D.; de Volder, M.; Ahmad, S. Photo-Rechargeable LIBs: Device Configurations, Mechanisms, and Materials. *ACS Appl. Energy Mater.* **2022**, *5*, 7891–7912. [CrossRef]
115. Kin, L.; Liu, Z.; Astakhov, O.; Agbo, S.N.; Tempel, H.; Yu, S.; Kungl, H.; Eichel, R.-A.; Rau, U.; Kirchartz, T.; et al. Efficient Area Matched Converter Aided Solar Charging of LIBs Using High Voltage PSCs. *ACS Appl. Energy Mater.* **2020**, *3*, 431–439. [CrossRef]
116. Gurung, A.; Chen, K.; Khan, R.; Abdulkarim, S.S.; Varnekar, G.; Pathak, R.; Naderi, R.; Qiao, Q. Highly Efficient Perovskite Solar Cell Photocharging of Li-ion Battery Using DC-DC Booster. *Adv. Energy Mater.* **2017**, *7*, 1602105. [CrossRef]
117. Bi, J.; Zhang, J.; Giannakou, P.; Wickramanayake, T.; Yao, X.; Wang, M.; Liu, X.; Shkunov, M.; Zhang, W.; Zhao, Y. A Highly integrated flexible photo-rechargeable system based on stable ultrahigh-rate quasi-solid-state zinc-ion micro-batteries and PSCs. *Energy Storage Mater.* **2022**, *51*, 239–248. [CrossRef]
118. Chen, P.; Li, T.-T.; Yang, Y.-B.; Li, G.-R.; Gao, X.-P. Coupling aqueous zinc batteries and PSCs for simultaneous energy harvest, conversion and storage. *Nat. Commun.* **2022**, *13*, 64. [CrossRef] [PubMed]
119. Cui, C.; Wang, X.; Zhu, H.; Jin, Y.; Li, Y.; Pang, B.; Shang, M.; Dong, H.; Yu, L.; Dong, L. Photo-assisted enhancement of Li-ion battery performance with a $\text{LiFePO}_4/\text{TiO}_2$ composite cathode. *Ceram. Int.* **2024**, *50*, 11291–11297. [CrossRef]
120. Chen, Y.; Chen, Z.; Zhang, X.; Chen, J.; Wang, Y. An organic-halide perovskite-based photo-assisted Li-ion battery for photoelectrochemical storage. *Nanoscale* **2022**, *14*, 10903–10909. [CrossRef] [PubMed]
121. Tuc Altaf, C.; Rostas, A.M.; Popa, A.; Toloman, D.; Stefan, M.; Demirci Sankir, N.; Sankir, M. Recent Advances in Photochargeable Integrated and All-in-One Supercapacitor Devices. *ACS Omega* **2023**, *8*, 47393–47411. [CrossRef] [PubMed]
122. Xu, X.; Li, S.; Zhang, H.; Shen, Y.; Zakeeruddin, S.M.; Graetzel, M.; Cheng, Y.-B.; Wang, M. A Power Pack Based on Organometallic Perovskite Solar Cell and Supercapacitor. *ACS Nano* **2015**, *9*, 1782–1787. [CrossRef] [PubMed]
123. Li, H.; Chen, C.; Hu, H.; Li, Y.; Shen, Z.; Li, F.; Liu, Y.; Liu, R.; Chen, J.; Dong, C.; et al. Strategies for high-performance PSCs from materials, film engineering to carrier dynamics and photon management. *InfoMat* **2022**, *4*, e12322. [CrossRef]
124. Tewari, N.; Shivarudraiah, S.B.; Halpert, J.E. Photorechargeable Lead-Free Perovskite LIBs Using Hexagonal $\text{Cs}_3\text{Bi}_2\text{I}_9$ Nanosheets. *Nano Lett.* **2021**, *21*, 5578–5585. [CrossRef]
125. Li, C.; Cong, S.; Tian, Z.; Song, Y.; Yu, L.; Lu, C.; Shao, Y.; Li, J.; Zou, G.; Rümmeli, M.H.; et al. Flexible perovskite solar cell-driven photo-rechargeable Li-ion capacitor for self-powered wearable strain sensors. *Nano Energy* **2019**, *60*, 247–256. [CrossRef]
126. Zheng, D.; Sun, X.; An, C.; Pan, F.; Qin, C.; Wang, Z.; Deng, Q.; Song, Y.; Li, Y. Flexible multi-layered porous CuxO/NiO ($x = 1, 2$) photo-assisted electrodes for hybrid supercapacitors: Design and mechanism insight. *Chem. Eng. J.* **2023**, *473*, 145289. [CrossRef]
127. Dang, C.; He, S.; Liu, Y.; Zhao, L.; Shan, A.; Li, M.; Kong, L.; Gao, L. Designing $\text{In}_2\text{S}_3@\text{Bi}_2\text{S}_3$ type II heterostructure for bifunctional photo-enhanced Li-O_2 batteries. *Chem. Eng. J.* **2023**, *476*, 146775. [CrossRef]

Disclaimer/Publisher's Note: The statements, opinions and data contained in all publications are solely those of the individual author(s) and contributor(s) and not of MDPI and/or the editor(s). MDPI and/or the editor(s) disclaim responsibility for any injury to people or property resulting from any ideas, methods, instructions or products referred to in the content.